



Published in final edited form as:

Nature. 2019 March ; 567(7747): 249–252. doi:10.1038/s41586-019-1004-y.

Hepatocytes direct the formation of a pro-metastatic niche in the liver.

Jae W. Lee^{1,2}, Meredith L. Stone^{1,2}, Paige M. Porrett³, Stacy K. Thomas^{1,2}, Chad A. Komar^{1,2}, Joey H. Li^{1,2}, Devora Delman^{1,2}, Kathleen Graham^{1,2}, Whitney L. Gladney^{1,2}, Xia Hua^{1,2}, Taylor A. Black^{1,2}, Austin L. Chien^{1,2}, Krishna S. Majmundar^{1,2}, Jeffrey C. Thompson^{1,2}, Stephanie S. Yee^{1,2}, Mark H. O'Hara^{1,2}, Charu Aggarwal^{1,2}, Dong Xin³, Abraham Shaked³, Mingming Gao⁴, Dexi Liu⁴, Mitesh J. Borad⁵, Ramesh K. Ramanathan⁶, Erica L. Carpenter^{1,2}, Ailing Ji^{7,8}, Maria C. de Beer^{8,9}, Frederick C. de Beer^{7,8}, Nancy R. Webb^{8,10}, and Gregory L. Beatty^{1,2}

¹Abramson Cancer Center; University of Pennsylvania, Philadelphia, Pennsylvania 19104;

²Division of Hematology-Oncology, Department of Medicine, Perelman School of Medicine, University of Pennsylvania, Philadelphia, Pennsylvania 19104;

³Division of Transplant Surgery, Department of Surgery, Perelman School of Medicine, University of Pennsylvania, Philadelphia, Pennsylvania 19104;

⁴Department of Pharmaceutical and Biomedical Sciences, College of Pharmacy, University of Georgia, Athens, Georgia 30602;

⁵Mayo Clinic Cancer Center; Mayo Clinic, Phoenix, Arizona 85054;

⁶Mayo Clinic Cancer Center; Mayo Clinic, Phoenix, Arizona 85054; present address Merck Research Labs, Rahway, NJ 07065

⁷Department of Internal Medicine, University of Kentucky, Lexington, Kentucky 40536;

⁸Saha Cardiovascular Research Center; University of Kentucky, Lexington, Kentucky 40536;

⁹Department of Physiology, University of Kentucky, Lexington, Kentucky 40536;

Users may view, print, copy, and download text and data-mine the content in such documents, for the purposes of academic research, subject always to the full Conditions of use: http://www.nature.com/authors/editorial_policies/license.html#terms Reprints and permissions information is available at www.nature.com/reprints.

Correspondence and requests for materials should be addressed to G.L.B. (gregory.beatty@uphs.upenn.edu).

Author Contributions

Experiments and data analysis were performed by J.W.L., M.L.S., P.M.P., S.K.T., C.A.K., D.D., W.L.G., X.H., A.J., M.C.d.B., F.C.d.B., N.R.W., and G.L.B.; generation of mouse pancreatic tumor cell lines by W.L.G. and G.L.B.; immunofluorescence and immunohistochemistry by J.W.L., M.L.S., J.H.L., D.D., W.L.G., and A.J.; RNA *in situ* hybridization by J.W.L. and X.H.; tumor cell culture by J.W.L., M.L.S., and C.A.K.; animal studies by J.W.L., M.L.S., S.K.T., C.A.K., K.G., and W.L.G.; flow cytometry by J.W.L., M.L.S., and S.K.T.; QuantSeq 3' mRNA sequencing and data analysis by J.W.L.; quantitative real-time PCR by J.W.L., J.H.L., and X.H.; cytokine bead array by J.W.L., M.L.S., and C.A.K.; primary hepatocyte studies by J.W.L.; enzyme-linked immunosorbent assays by J.W.L. and M.C.d.B.; hydrodynamic injection studies by J.W.L., D.L., and M.G.; parabiotic joining by J.W.L. and P.M.P. M.C.d.B., F.C.d.B., and N.R.W. provided *Saa*^{-/-} mice; D.X. and A.S. provided liver specimens from normal donors; M.J.B. and R.K.R. provided liver specimens from PDAC patients; T.A.B., A.L.C., K.S.M., J.C.T., S.S.Y., M.O., C.A., and E.L.C. provided plasma samples; M.G. established hydrodynamic injection procedure; D.L. designed and prepared IL-6 expression vector; P.M.P., M.G., D.L., E.L.C., M.C.d.B., F.C.d.B., and N.R.W. provided experimental advice; J.W.L. and G.L.B. designed the study; J.W.L., M.L.S., and G.L.B. prepared and wrote the manuscript.

The authors have no competing financial interests.

¹⁰Department of Pharmacology and Nutritional Sciences, University of Kentucky, Lexington, Kentucky 40536

Abstract

The liver is the most common site of metastatic disease¹. While this metastatic tropism may reflect mechanical trapping of circulating tumor cells, liver metastasis is also dependent, at least in part, on formation of a “pro-metastatic” niche that supports tumor cell spread to the liver^{2,3}. Mechanisms that direct formation of this niche, though, are poorly understood. Here, we show that hepatocytes coordinate myeloid cell accumulation and fibrosis within the liver, and in doing so, increase the susceptibility of the liver to metastatic seeding and outgrowth. Early during pancreatic tumorigenesis, hepatocytes demonstrate activation of Signal Transducer and Activator of Transcription 3 (STAT3) signaling and increased production of serum amyloid A1 and A2 (SAA). Overexpression of SAA by hepatocytes also occurs in pancreatic and colorectal cancer patients with liver metastases, and many patients with locally advanced and metastatic disease display elevated levels of circulating SAA. STAT3 activation in hepatocytes and the subsequent production of SAA are dependent on interleukin 6 (IL-6) that is released into the circulation by non-malignant cells. Genetic ablation or blockade of components of IL-6/STAT3/SAA signaling prevents establishment of a pro-metastatic niche and inhibits liver metastasis. Our data reveal an intercellular network underpinned by hepatocytes that forms the basis for a pro-metastatic niche in the liver and identify new therapeutic targets.

Main Text

To understand mechanisms underlying formation of a pro-metastatic niche in the liver, we utilized the *LSL-Kras^{G12D/+};LSL-Trp53^{R127H/+};Pdx-1-Cre* (KPC) mouse model of pancreatic ductal adenocarcinoma (PDAC)^{4,5}. We examined for features of a pro-metastatic niche in the liver of tumor-bearing (TB) KPC mice and 8- to 10-week-old non-tumor-bearing (NTB) KPC mice, which lack PDAC but harbor pancreatic intraepithelial neoplasia (PanIN)⁶. Compared to control mice, KPC mice demonstrated increased numbers of myeloid cells, accompanied by an increase in the deposition and expression of fibronectin (FN) and type I collagen (COL1) (Fig. 1a and Extended Data Fig. 1a-d). Orthotopic implantation of KPC-derived PDAC cells into wild type mice recapitulated these changes (Extended Data Fig. 1e-i). Similar to prior studies^{7,8}, we also found that matrix deposition did not require myeloid cells (Extended Data Fig. 1j-l). These results are consistent with studies showing myeloid cell accumulation and extracellular matrix deposition as key components of a pro-metastatic niche⁷⁻¹⁰.

We next evaluated the susceptibility of the liver to metastatic colonization. YFP-labeled KPC-derived PDAC cells (PDAC-YFP)⁶ were injected into control mice and KPC mice. Metastatic burden was three-fold higher in KPC mice, and metastatic lesions were detected in the liver of KPC mice at increased frequency and size with enhanced proliferation (Ki-67) (Fig. 1b and Extended Data Fig. 2a, b). Similar findings were observed using a YFP-negative KPC-derived cell line (Extended Data Fig. 2c, d). Orthotopic implantation of PDAC cells also increased the susceptibility of the liver to metastatic colonization, and this finding was independent of T cells (Extended Data Fig. 2e-s).

We next performed mRNA sequencing on RNA isolated from the liver of control and KPC mice. We identified 275 differentially expressed genes (Extended Data Fig. 3a, b and Supplementary Data 1) and found that genes upregulated in KPC mice were associated with immune-related processes (Extended Data Fig. 3c). Notably, we found an upregulation of myeloid chemoattractants in KPC mice (Fig. 1c and Extended Data Fig. 3d, e), including *Saa* as well as *S100* genes^{11–13}. We also found an enrichment of immune-related pathways, particularly the IL-6/JAK/STAT3 signaling pathway (Extended Data Fig. 3f). We validated our results by examining the liver of KPC mice for the presence of phosphorylated STAT3 (pSTAT3). Remarkably, 80–90% of hepatocytes displayed STAT3 activation in KPC mice, compared to <2% of hepatocytes in control mice (Extended Data Fig. 3g, h). In contrast, we did not detect activation of STAT1 signaling (Extended Data Fig. 3i). Orthotopic implantation of PDAC cells also induced phosphorylation of STAT3 in hepatocytes (Extended Data Fig. 3j–k).

As IL-6 is fundamental to STAT3 signaling in hepatocytes¹⁴, we examined the liver of control mice (*Il-6*^{+/+}) and IL-6 knockout mice (*Il-6*^{-/-}) orthotopically injected with PBS or PDAC cells. Tumor-implanted *Il-6*^{-/-} mice displayed a decrease in STAT3 activation, particularly in hepatocytes (Fig. 2a and Extended Data Fig. 4a). This loss in STAT3 activation was accompanied by reduced myeloid cell accumulation as well as extracellular matrix deposition without alterations in the morphology and density of liver sinusoids (Fig. 2a and Extended Data Fig. 4a–d). We also observed reduced expression of SAA, other chemoattractants, and extracellular matrix proteins (Fig. 2b and Extended Data Fig. 4e). Genetic ablation of *Il-6*, however, did not impact proliferation, vascular density, or primary tumor growth (Extended Data Fig. 4f, g). *Il-6*^{-/-} mice were also less susceptible to metastatic colonization, and blockade of IL-6 receptor (IL-6R) similarly inhibited formation of a pro-metastatic niche in the liver (Fig. 2c–e and Extended Data Fig. 4h–s). Intriguingly, genetic ablation of *Il-6* or blockade of IL-6R did not completely inhibit STAT3 signaling, suggesting that IL-6-independent mechanisms may contribute to STAT3 activation.

IL-6 promotes development and progression of PDAC^{15–18}. To identify the source of IL-6, we orthotopically injected PBS or PDAC cells into *Il-6*^{+/+} and *Il-6*^{-/-} mice and determined the concentration of IL-6 in distinct anatomic sites (Extended Data Fig. 5a). We detected IL-6 only in tumor-implanted *Il-6*^{+/+} mice, with the highest concentration of IL-6 found in the primary tumor (Extended Data Fig. 5b, c). While *Il-6* mRNA was undetectable in the liver, lung, and malignant cells, we observed *Il-6* mRNA in host cells located adjacent to CK19-expressing PDAC cells (Extended Data Fig. 5d–g). Human primary tumors displayed a similar expression pattern (Extended Data Fig. 5h). Moreover, *Il-6* mRNA was detected in α -SMA⁺ stromal cells located adjacent to PanIN and PDAC cells in KPC mice (Extended Data Fig. 5i–k). We also found that primary pancreatic tumor supernatant activated STAT3 signaling in hepatocytes which was reduced in the presence of anti-IL-6R antibodies (Extended Data Fig. 6a, b). These results show that IL-6 released by non-malignant cells within the primary tumor is a key mediator of STAT3 signaling in hepatocytes.

To study a role for hepatocytes in directing liver metastasis, we generated mice that lack *Stat3* in hepatocytes (*Stat3*^{flox/flox} *Alb-Cre*). Compared to control mice (*Stat3*^{flox/flox}), tumor-implanted *Stat3*^{flox/flox} *Alb-Cre* mice lacked features of a pro-metastatic niche (Fig.

3a-c and Extended Data Fig. 6c) and failed to produce SAA (Fig. 3d-f). However, deletion of *Stat3* in hepatocytes did not affect liver sinusoid density or morphology and did not alter the size, proliferation, or vascular density of the primary tumor (Extended Data Fig. 6d-f). The liver of tumor-implanted *Stat3^{flox/flox} Alb-Cre* mice was also less susceptible to metastatic colonization (Extended Data Fig. 6g-l). In addition to its expression in hepatocytes (Extended Data Fig. 6m), *Saa* mRNA was detected in colonic cells¹⁹ and in cells present in the periphery of the primary tumor (Extended Data Fig. 6n). However, both cell types maintained comparable levels of *Saa* mRNA despite deletion of *Stat3* in hepatocytes.

SAA proteins are acute phase reactants²⁰. Consistent with elevated levels of circulating SAA in tumor-implanted mice (Fig. 3f), PDAC patients displayed elevated levels of circulating SAA (Extended Data Fig. 7a). Overexpression of SAA and pSTAT3 by hepatocytes was also observed in 5 of 7 patients with liver metastases (Fig. 4a and Extended Data Fig. 7b). Notably, high levels of circulating SAA correlated with worse outcomes (Extended Data Fig. 7c). Elevated levels of circulating SAA were also observed in non-small cell lung carcinoma (NSCLC) patients with liver metastases, and SAA overexpression by hepatocytes was detected in the liver of colorectal carcinoma (CRC) patients (Extended Data Fig. 7d, e). In addition, compared to tumor-implanted control mice (*Saa^{+/+}*), *Saa^{-/-}* mice implanted with PDAC or MC-38 CRC cells failed to show features of a pro-metastatic niche in the liver, though genetic ablation of *Saa* had no impact on primary tumor growth (Fig. 4b-e and Extended Data Fig. 7f-s). SAA was also necessary for IL-6-mediated formation of a pro-metastatic niche as well as for fibrosis and myeloid cell recruitment in the setting of liver injury (Extended Data Fig. 8).

Tissue inhibitor of metalloproteinases 1 (TIMP1)^{7,8} and macrophage migration inhibitory factor (MIF)^{9,10} have been implicated in promoting metastasis. However, expression of these molecules were not affected by IL-6/STAT3/SAA signaling (Extended Data Fig. 9). We next determined whether formation of a pro-metastatic niche in the liver is dependent on the anatomic proximity of the pancreas to the liver. To do so, we examined for features of a pro-metastatic niche in the liver of CD45.1 and CD45.2 mice that were parabiotically joined (Extended Data Fig. 10a). Though only CD45.2 mice were implanted with PDAC cells, both mice displayed myeloid cell accumulation and fibrosis in the liver (Extended Data Fig. 10b-f), suggesting that formation of this niche is not dependent on the anatomic distance between tumor and liver. We also examined a role for SAA in establishing a pro-metastatic niche in the lung. PDAC development in KPC mice induced Ly6G⁺ myeloid cell accumulation and deposition of FN within the lung, yet IL-6/STAT3/SAA signaling was not required for formation of a pro-metastatic niche in the lung (Extended Data Fig. 10h-o).

Our data provide novel insight into the mechanisms that direct liver metastasis. While recent works have suggested a role for tumor-intrinsic factors in driving metastatic spread of cancer^{7-10,21-23}, we provide the first evidence that inflammatory responses mounted by hepatocytes are critical to liver metastasis. Mechanistically, hepatocytes orchestrate this process through activation of IL-6/STAT3 signaling and the subsequent production of SAA, which alters the immune and fibrotic microenvironment of the liver to establish a pro-metastatic niche (Extended Data Fig. 10p). Our findings argue for therapies that target hepatocytes for preventing liver metastasis in cancer.

METHODS

Animals

CD45.2 (wild type, C57BL/6J), CD45.1 (B6.SJL-*Ptprca*^a *Pepc*^b/BoyJ), *Il-6* knockout (*Il-6*^{-/-}, B6.129S2-*Il6*^{tm1Kopf}/J), *Stat3*^{flox/flox} (B6.129S1-*Stat3*^{tm1Xyfu}/J), and *Albumin-Cre*^{+/+} (B6.Cg-Tg(Alb-cre)21Mgn/J) mice were obtained from the Jackson Laboratory. *Stat3*^{flox/flox} mice were bred to *Albumin-Cre*^{+/+} mice to generate *Stat3*^{flox/+} *Albumin-Cre*^{+/+} mice, which were backcrossed onto *Stat3*^{flox/flox} mice to generate *Stat3*^{flox/flox} *Albumin-Cre*^{+/+} mice. These mice were then bred to each other to create *Stat3*^{flox/flox} *Albumin-Cre*^{+/+} and *Stat3*^{flox/flox} *Albumin-Cre*^{+/-} mice (*Stat3*^{flox/flox} Alb-Cre), and *Stat3*^{flox/flox} *Albumin-Cre*^{-/-} mice (*Stat3*^{flox/flox}). *Kras*^{LSL-G12D/+}; *Trp53*^{LSL-R172H/+}; *Pdx1-Cre* (KPC) mice and *Trp53*^{LSL-R172H/+}; *Pdx1-Cre* (PC) mice were previously described^{4,5}. *Saa1* and *Saa2* double knockout (*Saa*^{-/-}) mice were previously described²⁴ and provided by the University of Kentucky College of Medicine. *Saa*^{-/-} mice used for experiments had been bred to obtain a 99.9% C57BL/6 background using the Jackson Laboratory Speed Congenic Service²⁴. All transgenic mice were bred and maintained in the animal facility of the University of Pennsylvania. Animal protocols were reviewed and approved by the Institute of Animal Care and Use Committee of the University of Pennsylvania. In general, mice were monitored three times per week for general health and euthanized early based on defined endpoint criteria including tumor diameter \geq 1 cm, ascites, lethargy, loss of \geq 10% body weight, or other signs of sickness or distress.

Clinical Samples

All patient samples were obtained after written informed consent and were de-identified. Studies were conducted in accordance with the 1996 Declaration of Helsinki and approved by institutional review boards of the University of Pennsylvania and the Mayo Clinic. To obtain the plasma from normal donors, PDAC patients, and NSCLC patients, peripheral whole blood was drawn in EDTA tubes (Fisher Scientific). Within 3 hours of collection, blood samples were centrifuged at $1,600 \times g$ at room temperature for 10 minutes with the brake off. Next, the plasma was transferred to a 15-mL conical tube without disturbing the cellular layer and centrifuged at $3,000 \times g$ at room temperature for 10 minutes with the brake off. This step was repeated with a fresh 15-mL conical tube. The plasma was then stored at -80°C until analysis. Biopsy results, computed tomography, and/or magnetic resonance imaging records were used to determine sites of metastasis in PDAC patients and NSCLC patients whose plasma samples were used for assessment of SAA levels. Liver specimens from normal donors were obtained by percutaneous liver biopsy, and acquisition of liver specimens from patients with liver metastases was previously described²⁵. Liver specimens from CRC patients with liver metastases were obtained from the Cooperative Human Tissue Network (CHTN). Patient characteristics are shown in Supplementary Table 2.

Cell Lines

PDA.69 cell line (PDAC cells) was used for intrasplenic and orthotopic injection, and PDA.8572 cell line (PDAC-YFP cells) was used for intrasplenic, intraportal, and retro-orbital injections. These cell lines were derived from PDAC tumors spontaneously arising in KPC mice, as previously described^{4,26}. MC-38 cell line, which was used for orthotopic

implantation, was purchased from Kerafast. Cell lines were cultured in DMEM (Corning) supplemented with 10% fetal bovine serum (FBS, VWR), 83 µg/mL gentamicin (Thermo Fisher), and 1% GlutaMAX (Thermo Fisher) at 37 °C, 5% CO₂. Only cell lines that had been passaged less than 10 times were used for experiments, and trypan blue staining was used to ensure that cells with > 95% viability were used for studies. Cell lines were tested routinely for *Mycoplasma* contamination at the Cell Center Services Facility at the University of Pennsylvania. All cell lines used in our studies tested negative for *Mycoplasma* contamination.

Animal Experiments

For all animal studies, mice of similar age and gender were block randomized in an unblinded fashion. Male and female mice aged between 8 to 12 weeks were used unless indicated otherwise. Mice were age- and gender-matched with appropriate control mice for analysis. Sample sizes were estimated based on pilot experiments and were selected to provide sufficient numbers of mice in each group for statistical analysis.

For orthotopic and intrasplenic injections of pancreatic tumor cells, mice were anesthetized using continuous isoflurane, and their abdomen was sterilized. After administering analgesic agents and assessing the depth of anesthesia, laparotomy (5–10 mm) was performed over the left upper quadrant of the abdomen to expose the peritoneal cavity. For orthotopic injection, the pancreas was exteriorized onto a sterile field, and sterile PBS or pancreatic tumor cells (5×10^5 cells suspended in 50 µL of sterile PBS) were injected into the tail of the pancreas via a 30-gauge needle (Covidien). Successful injection was confirmed by the formation of a liquid bleb at the site of injection with minimal fluid leakage. The pancreas was then gently placed back into the peritoneal cavity. For intrasplenic injection, 150 µL of sterile PBS was drawn into a syringe then sterile PBS or pancreatic tumor cells (5×10^5 cells suspended in 100 µL of sterile PBS) were gently drawn into the same syringe in an upright position as previously described²⁷. After exteriorizing the spleen onto a sterile field, pancreatic tumor cells were injected into the spleen via a 30-gauge needle. Successful injection was confirmed by whitening of the spleen and splenic blood vessels with minimal leakage of content into the peritoneum. Splenectomy was then performed by ligating splenic vessels with clips (Horizon) then cauterizing them to ensure that there was no hemorrhage. Afterwards, the remaining blood vessels were placed back into the peritoneal cavity. For both procedures, the peritoneum was closed with a 5-0 PDS II violet suture (Ethicon), and the skin was closed using the AutoClip system (Braintree Scientific). Following surgery, mice were given buprenorphine subcutaneously at a dose of 0.05–0.1 mg/kg every 4–6 hours for 12 hours and then every 6–8 hours for 3 additional days. Mice that were orthotopically injected with pancreatic tumor cells were analyzed after 20 days, unless indicated otherwise in study designs. Mice that were intrasplenically injected with PDAC cells were analyzed after 10 days.

For intraportal injection of pancreatic tumor cells and hydrodynamic injection of expression vectors, mice were anesthetized using continuous isoflurane, and their abdomen was sterilized. After administration of analgesic agents, median laparotomy (10 mm) was performed, and the incision site was held open using an Agricola retractor (Roboz). After

exposure of the peritoneal cavity, the intestines were located and exteriorized onto a sterile field surrounding the incision site to visualize the portal vein. Throughout the procedure, the intestines were kept hydrated with sterile PBS that was pre-warmed at 37 °C. For intraportal injection, sterile PBS or pancreatic tumor cells (5×10^5 cells suspended in 100 μ L of sterile PBS) were injected into the portal vein via a 30-gauge needle. Successful injection was confirmed by partial blanching of the liver. For hydrodynamic injection, 1 μ g of pLIVE expression vectors were suspended in sterile saline corresponding to 8% of mouse body weight as previously described²⁸. Vectors were injected into the portal vein via a 27-gauge needle within 5–8 seconds. Successful injection was confirmed by complete blanching and swelling of the liver. For both procedures, a sterile gauge was then held over the injection site for 1 minute to ensure that no injected contents would leak into the peritoneal cavity. Afterwards, the intestines were placed back into the peritoneal cavity, and the peritoneum and skin were closed with a suture and autoclips, respectively. Following surgery, mice were given buprenorphine subcutaneously as described above. Intraportal injection of pancreatic tumor cells was performed on day 10, and metastatic burden in the liver was evaluated on day 20, unless indicated otherwise in study designs.

For orthotopic implantation of colorectal tumor cells, wild type mice were first subcutaneously injected with MC-38 (1×10^6 cells suspended in 100 μ L of sterile PBS) on the right flank. After 10 days, mice were euthanized, and subcutaneous tumors were collected. Tumors were then cut into small pieces, each 3 \times 3 mm in size, and placed in sterile PBS on ice until implantation. Mice were anesthetized using isoflurane, and their abdomen was sterilized. Following administration of analgesic agents, median laparotomy was performed as described above. Implantation of colorectal tumor tissues into the cecum was then performed as previously described²⁹. After placing the intestines back into the peritoneal cavity, the peritoneum and skin were closed with a suture, and mice were given buprenorphine as described above. Mice were analyzed after 10 days.

For parabiotic joining of mice, female CD45.2 mice were orthotopically injected with sterile PBS or pancreatic tumor cells as described above and co-housed with age-matched female B6 CD45.1 mice. Each parabiotic pair was housed in a separate cage to maximize bonding between partners. After one week, parabiotic partners were anesthetized using continuous isoflurane, and their flanks were sterilized. After administration of analgesic agents, longitudinal skin flaps from the lower limb to the upper limb were created, and everted skin flaps were sewn using a suture. In addition, the knees and olecranon of parabiotic partners were joined together using a suture for additional stabilization. Following surgery, mice were given buprenorphine subcutaneously at a dose of 0.05–0.1 mg/kg every 4–6 hours for 5 days. Parabiotically joined mice were analyzed after 20 days.

For administration of antibodies, the abdomen of mice was sterilized, and anti-CD4 antibodies (GK1.5, 0.2 mg), anti-CD8 antibodies (2.43, 0.2 mg), anti-IL-6R antibodies (15A7, 0.2 mg), or rat isotype control antibodies (LTF-2, 0.2 mg) were suspended in 100 μ L of sterile PBS. Antibodies were subsequently injected into the peritoneum via a 30-gauge needle. All antibodies used in *in vivo* experiments were obtained from BioXCell. To deplete F4/80⁺ myeloid cells, clodronate-encapsulated liposomes (Liposoma) were administered through intraperitoneal injection according to manufacturer's protocol. For induction of liver

injury, mice were intraperitoneally injected with CCl₄ (Sigma, 1 mL/kg of body weight) dissolved in sunflower seed oil as previously described³⁰. Detailed information on antibodies and reagents used in experiments can be found in Supplementary Table 3.

Microscopic analysis

For preparation of formalin-fixed paraffin-embedded (FFPE) sections, dissected tissues were fixed in 10% formalin for 24 hours at room temperature, washed two times with PBS, and then stored in 70% ethanol solution at 4 °C until they were embedded in paraffin and sectioned at 5 µm. For preparation of cryosections, dissected tissues were embedded in Tissue-tek O.C.T. (Electron Microscopy Sciences) and frozen on dry ice. Frozen tissues were stored at -80 °C until they were sectioned at 7 µm.

Automated immunohistochemistry, immunofluorescence, and RNA *in situ* hybridization were performed on FFPE sections using a Ventana Discovery Ultra automated slide staining system (Roche). Reagents were obtained from Roche and ACDBio (Supplementary Table 3) and used according to manufacturer's protocol. Images were acquired using a BX43 upright microscope (Olympus), an Aperio CS2 scanner system (Leica), or an IX83 inverted multicolor fluorescent microscope (Olympus). Manual immunohistochemistry of mouse tissues for SAA was previously described³¹. For manual multicolor immunofluorescence staining, O.C.T. liver cryosections were briefly air dried and fixed with 3% formaldehyde at room temperature for 15 minutes. For intracellular staining, sections were permeabilized with methanol at -20 °C for 10 minutes immediately following formaldehyde fixation. Sections were then blocked with 10% normal goat serum in PBS containing 0.1% TWEEN 20 for 30 minutes. For intracellular staining, 0.3% Triton X-100 was added to the blocking solution for permeabilization of cellular and nuclear membranes. Sections were incubated with primary antibodies (Supplementary Table 3) in the blocking solution for 1 hour at room temperature or overnight at 4 °C, followed by washing with PBS containing 0.1% TWEEN 20. Sections were then incubated with secondary antibodies (Supplementary Table 3) in the blocking solution for 1 hour at room temperature or overnight at 4 °C. After washing, sections were stained with DAPI to visualize nuclei and subsequently with Sudan Black B in 70% ethanol to reduce autofluorescence, as previously described³². Immunofluorescence imaging was performed on an IX83 inverted multicolor fluorescent microscope (Olympus). For quantification of cells and extracellular matrix proteins, 5 random fields were acquired from each biological sample.

Flow Cytometry

Mice were euthanized, and the liver and lung were harvested after draining the blood by severing the portal vein and inferior vena cava. The liver and lung were rinsed thoroughly in PBS before mincing with micro dissecting scissors into small pieces (< 0.5 × 0.5 mm in size) at 4 °C in DMEM containing collagenase (1 mg/mL, Sigma-Aldrich), DNase (150 U/mL, Roche), and Dispase (1 U/mL, Worthington). Tissues were then incubated at 37 °C for 30 minutes with intermittent agitation, filtered through a 70-µm nylon strainer (Corning), and washed three times with DMEM. Cells were resuspended in ACK lysing buffer (Life Technologies) at room temperature for 15 minutes to remove red blood cells. After washing three times with DMEM, cells were counted and stained using Aqua dead cell stain kit (Life

Technologies) following manufacturer's protocol. For characterization of immune cell subsets, cells were washed three times with PBS containing 0.2 mM EDTA with 2% FBS and stained with appropriate antibodies (Supplementary Table 3). For quantification of PDAC-YFP cells, cells were not stained with any antibodies. Lastly, cells were washed three times with PBS containing 0.2 mM EDTA with 2% FBS and examined using a FACS Canto II (BD Biosciences). Collection and analysis of the peripheral blood was previously described²⁶. FlowJo (FlowJo, LLC, version 10.2) was used to analyze flow cytometric data and generate 2D t-SNE plots.

Detection of IL-6, SAA, and TIMP1

Mice that were orthotopically implanted with PDAC cells were euthanized, and primary tumors were harvested and weighed. In addition, blood samples were collected from the portal vein and left ventricle of the heart using a 27-gauge needle. Tumors were rinsed thoroughly in PBS and minced with micro dissecting scissors into small pieces ($< 0.5 \times 0.5$ mm in size) at 4 °C in serum-free DMEM at 1 mg of tissue per 1 μ L of medium. Tumor suspensions were then centrifuged at $12,470 \times g$ at 4 °C for 15 minutes, and tumor supernatant was collected and stored at -80 °C until analysis. Similar procedure was performed to obtain pancreas supernatant from mice that were orthotopically injected with PBS. To collect the serum, blood samples were allowed to clot at room temperature for 30 minutes. Samples were then centrifuged at $12,470 \times g$ at 4 °C for 15 minutes, and the serum was collected and stored at -80 °C until analysis. IL-6 levels in tumor/pancreas supernatant and serum were assessed using cytometric bead array (BD Biosciences) following manufacturer's protocol. Samples were examined using a FACS Canto II (BD Biosciences), and data were analyzed using FCAP Array (BD Biosciences, version 3.0). SAA and TIMP1 levels in mouse serum samples were measured using a commercially available enzyme-linked immunosorbent assay kit (Thermo Fisher) following manufacturer's protocol. Similarly, SAA levels in plasma samples collected from normal donors and PDAC patients as described under "Clinical Samples" were measured using a commercially available human enzyme-linked immunosorbent assay kit (Thermo Fisher) following manufacturer's protocol.

RNA and Quantitative Real-Time PCR

Mouse organs and cells were stored in TRIzol (Thermo Fisher) at -80 °C until analysis. Samples were thawed on ice and allowed to equilibrate to room temperature prior to isolating RNA using a RNeasy Mini kit (Qiagen) following manufacturer's protocol. cDNA synthesis was performed as previously described³³. Primers for quantitative real-time PCR were designed using the Primer3 online program⁴², and sequences were analyzed using the Nucleotide BLAST (NCBI) to minimize non-specific binding of primers. Primers were synthesized by Integrated DNA Technologies, and their sequences can be found in Supplementary Table 4. Quantitative real-time PCR was performed as previously described³³. Gene expression was calculated relative to *Actb* (β -actin) using the delta-Ct (Δ Ct) formula, and fold change in gene expression was calculated relative to the average gene expression of control groups using the delta delta Ct ($\Delta\Delta$ Ct) formula. Genes with Ct greater than or equal to 30 were considered not detected.

QuantSeq 3' mRNA Sequencing and Data Analysis

RNA was isolated from the liver of control mice and NTB KPC mice as described above and submitted to the Genomics Facility at the Wistar Institute. After assessing the quality of RNA using a 2100 Bioanalyzer (Agilent), samples were prepared using a QuantSeq 3' mRNA-Seq library prep kit FWD for Illumina (Lexogen) following manufacturer's protocol and analyzed on a NextSeq 500 sequencing system (Illumina). FASTQ files were uploaded to the BaseSpace Suite (Illumina) and aligned using its RNA-Seq Alignment application (version 1.0.0), in which STAR was selected to align sequences with maximum mismatches set to 14 as recommended by Lexogen. Output files were analyzed using Cufflinks Assembly & DE application (version 2.1.0) in the BaseSpace Suite to determine differentially expressed genes, which were used to generate an expression heatmap and a FPKM scatter plot. In addition, these genes were analyzed using ClueGO (version 2.3.3)³⁴ and CluePedia (version 1.3.3)³⁵, which are applications of Cytoscape software (version 3.5.1)³⁶. Functional group of biological processes were performed based on kappa score. Gene Ontology data^{37,38} downloaded on January 23, 2018 were used for analysis. Gene set enrichment analysis (version 3.0)³⁹ was used to determine biological processes that were differentially enriched in experimental groups.

In Vitro Studies

To isolate primary hepatocytes for *in vitro* studies, mice were anesthetized using continuous isoflurane, and their abdomen was sterilized. After administering analgesic agents and assessing the depth of anesthesia, laparotomy (10–15 mm) was performed along the midline of the abdomen to expose the peritoneal cavity. The intestines were then located and exteriorized to visualize the inferior vena cava and portal vein. The inferior vena cava was cannulated via a 24 gauge Insyte Autoguard catheter (BD), and the liver was perfused using 50 mL of liver perfusion medium (Thermo Fisher) at the flow rate of 8–9 mL/min using a peristaltic pump. At the start of perfusion, the portal vein was severed to drain the blood from the liver. Successful perfusion was confirmed by blanching of the liver, which was subsequently perfused using 50 mL of liver digest medium (Thermo Fisher) at the same flow rate. Both liver perfusion medium and liver digest medium were pre-warmed at 42 °C in a water bath. After perfusion, the liver was carefully transferred to a petri dish containing William's E medium (Sigma) supplemented with 10% FBS, 83 µg/mL gentamicin, and 1% GlutaMAX.

To dissociate hepatocytes from the liver, cell scrapers were used to create small cuts (5 mm) on the surface of the liver, and the tissue was gently shaken. Dissociated cells were then filtered through a 100-µm nylon strainer (Corning) and centrifuged at 50 × g at 4 °C for 5 minutes. After discarding the supernatant, cells were resuspended in a solution consisting of isotonic Percoll (Sigma) and supplemented William's E medium (2:3 ratio). Cells were then centrifuged at 50 × g at 4 °C for 10 minutes to obtain a pellet enriched in hepatocytes. After discarding the supernatant, hepatocytes were resuspended in supplemented William's E medium. Cell viability and number were determined using trypan blue staining, and 5 × 10⁴ hepatocytes were seeded on each well of a 48-well plate pre-coated with collagen. Hepatocytes were incubated in supplemented William's E medium for 4 hours at 37 °C, 5% CO₂ to allow attachment to the plate. Medium was then switched to HepatoZYME-SFM

(Thermo Fisher) supplemented with 83 µg/mL gentamicin and 1% GlutaMAX. Medium was replenished every 24 hours for the next 48 to 72 hours.

For hepatocyte activation assays, hepatocytes were incubated in supplemented HepatoZYME-SFM mixed with (i) serum-free DMEM, (ii) primary pancreatic tumor supernatant, or (iii) serum-free DMEM containing 250 ng/mL of IL-6 (Peprotech) for 30 minutes at 37 °C, 5% CO₂. All mixtures were made in a 1:1 ratio, and each condition was run in triplicates. For *in vitro* IL-6R blockade experiment, hepatocytes were pre-incubated with 5 µg/mL of anti-IL-6R antibodies for 2 hours prior to stimulating them with tumor supernatant. After stimulation, medium was carefully removed, and formaldehyde and methanol were used to fix and permeabilize hepatocytes, respectively, as described above. Hepatocytes were then stained for pSTAT3 (Supplementary Table 3), and their nuclei stained with DAPI. Immunofluorescence imaging was performed on an IX83 inverted multicolor fluorescent microscope (Olympus).

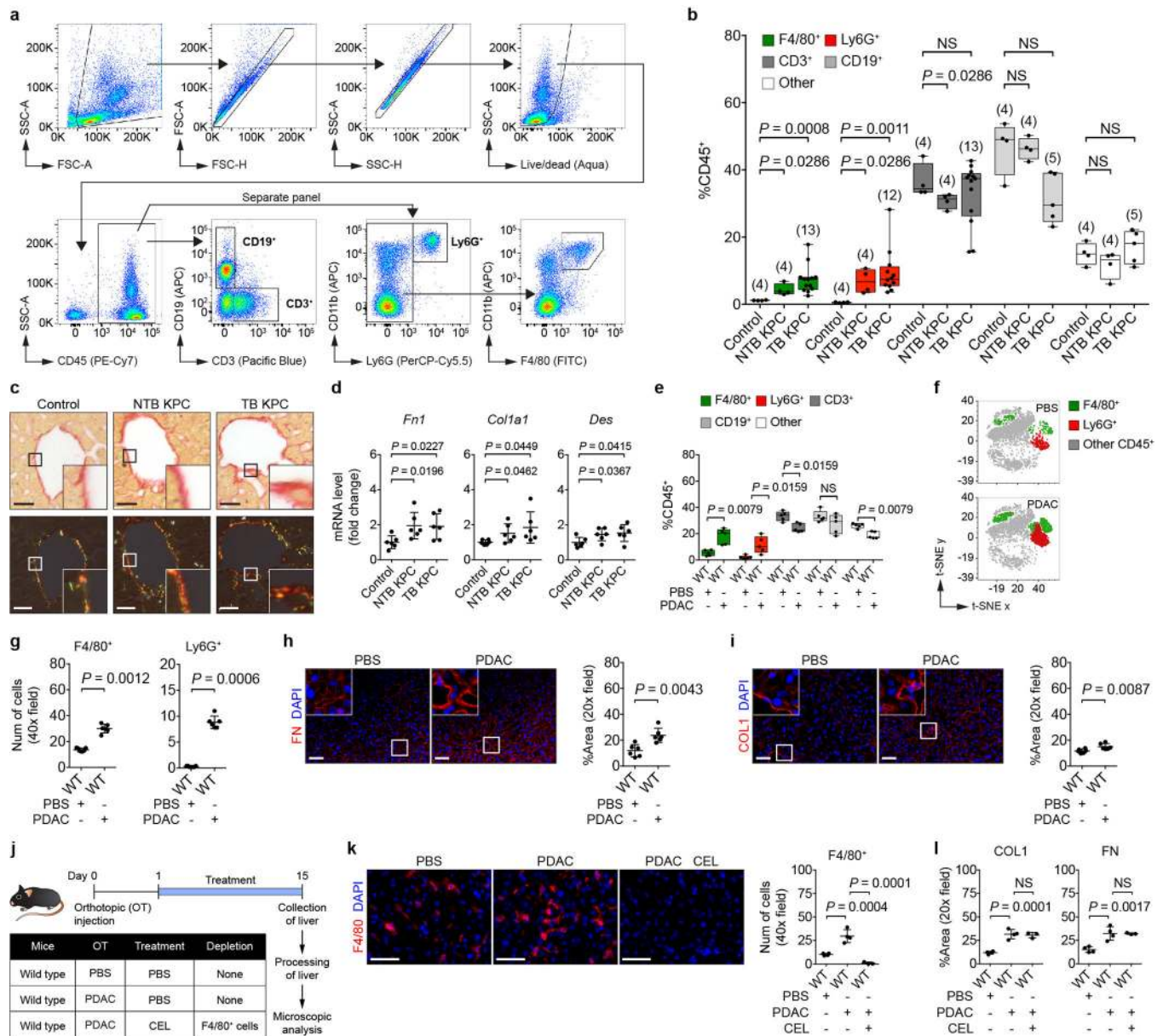
Statistical Analysis

Statistical significance was calculated using Prism (GraphPad Software, version 7) unless indicated otherwise. Multiple comparisons testing was performed using one-way ANOVA with Dunnett's test. Paired group comparisons test was carried out using two-tailed Wilcoxon matched-pairs signed rank test. Unpaired group comparisons test was performed using two-tailed unpaired Student's *t* test or two-tailed Mann-Whitney test. Comparison of Kaplan-Meier overall survival curves was performed using log-rank (Mantel-Cox) test. *P* values less than 0.05 were treated as significant.

Data availability

QuantSeq 3' mRNA sequencing data have been deposited in the Gene Expression Omnibus (GEO) under accession number GSE109480. Source data are provided for all figures and extended data figures. All data are available from the corresponding author upon reasonable request

Extended Data



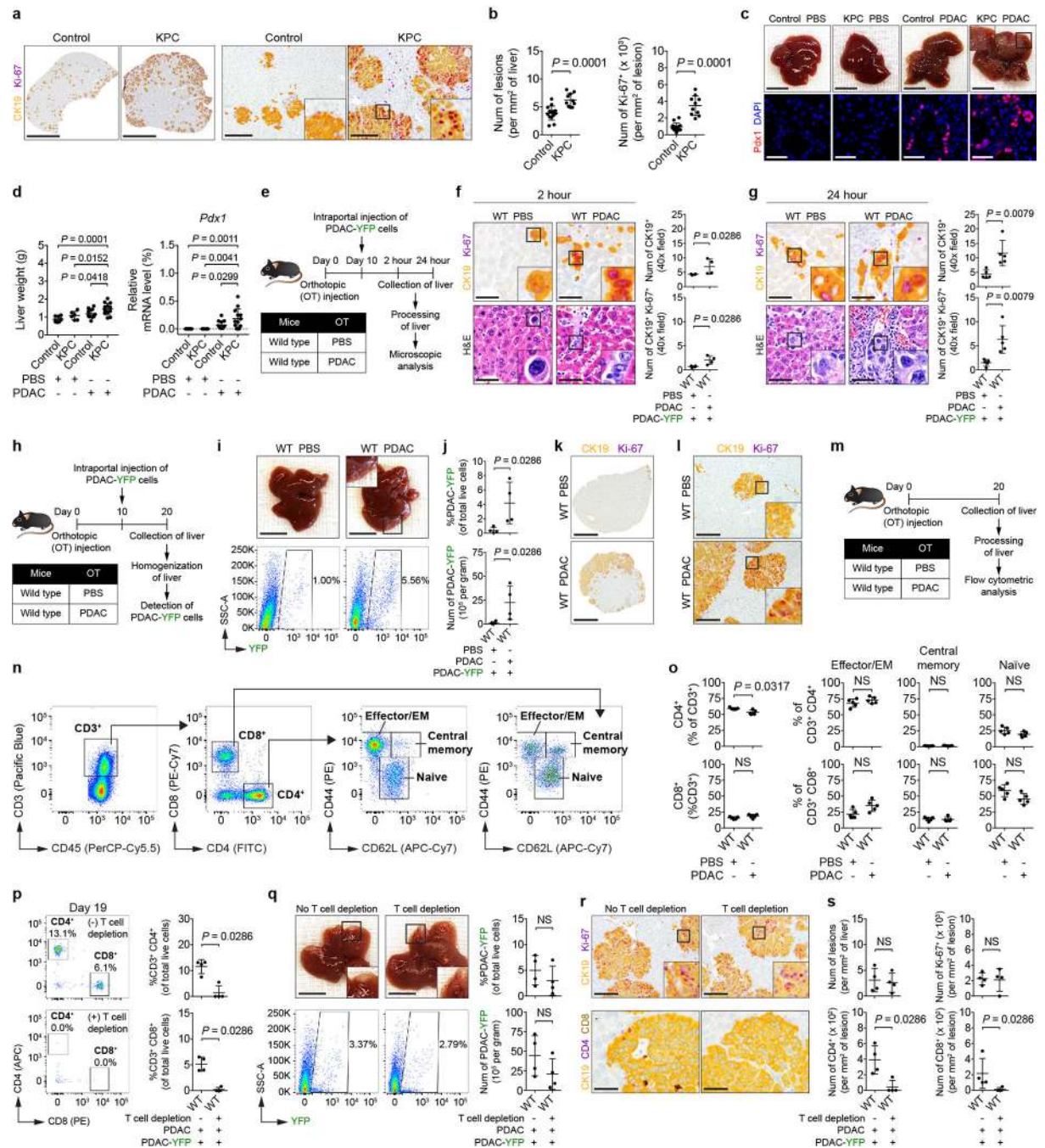
Extended Data Figure 1 | Primary PDAC development induces myeloid cell accumulation and fibrosis within the liver.

a, Gating strategy for identification of F4/80⁺, Ly6G⁺, CD3⁺, and CD19⁺ cells.

Representative images from flow cytometric analysis of cells isolated from the liver of a TB KPC mouse are shown. **b**, Quantification of immune cells in the liver by flow cytometry.

Numbers in parentheses indicate the number (n) of mice. Data pooled from four experiments. **c**, Representative Sirius red staining on the liver (n = 5 for all groups) viewed using standard light microscopy (top) and polarized light (bottom). **d**, mRNA levels of *Fn1*, *Col1a1*, and *Des* in the liver (n = 6 for all groups). Data pooled from two experiments (**c**, **d**). For **e-i**, wild type mice were orthotopically injected with PBS or PDAC cells and analyzed

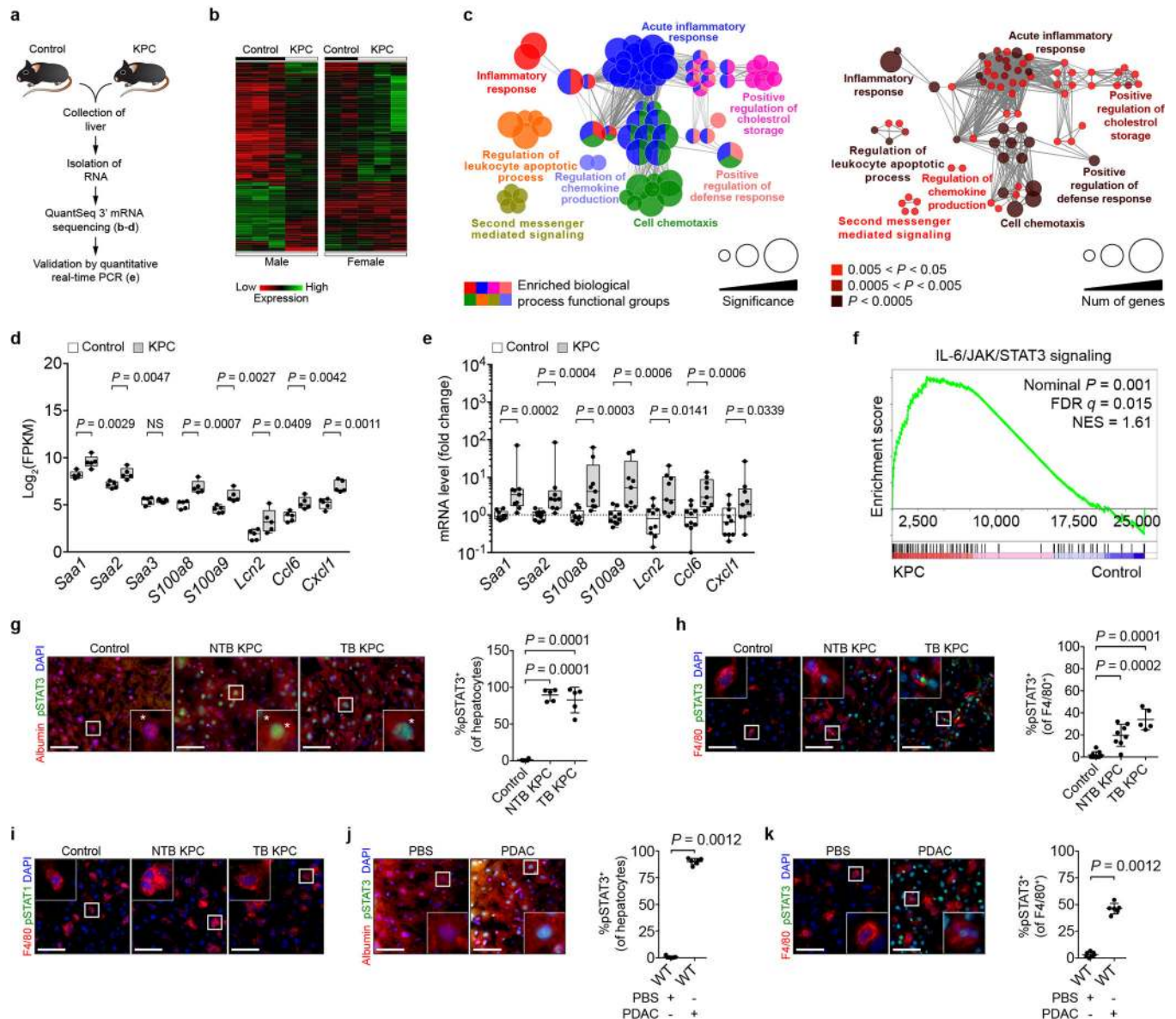
on day 20. **e**, Quantification of immune cells in the liver by flow cytometry ($n = 5$ for both groups). **f**, t-SNE 2D plots of immune cells analyzed in **e**. **g**, Quantification of myeloid cells in the liver ($n = 7$ for PBS and $n = 6$ for PDAC). **h**, **i**, Images and quantification of FN and COL1 in the liver ($n = 6$ for both groups). Data representative of at least two independent experiments (**e-i**). **j**, Study design for **k** and **l** ($n = 4$ for mice injected with PBS; $n = 4$ and 3 for mice injected with PDAC cells and then intraperitoneally injected with PBS and clodronate-encapsulated liposomes (CEL)). **k**, Images and quantification of F4/80⁺ cells in the liver. **l**, Quantification of COL1 and FN in the liver. Data representative of one experiment (**j-l**). Scale bars, 100 μm (**c**) and 50 μm (other panels). Statistical significance was calculated using two-tailed unpaired Student's t test (**d**), one-way ANOVA with Dunnett's test (**k**, **l**), and two-tailed Mann-Whitney test (all other panels). NS, not significant. Data represented as mean \pm s.d., except **b** and **e**, which are shown as box plots (center line, median; box limits, upper and lower quartiles; whiskers, max and min values).



Extended Data Figure 2 | Primary PDAC development enhances liver susceptibility to metastatic colonization.

For **a** and **b**, control mice ($n = 14$) and NTB KPC mice ($n = 10$) were intrasplenically injected with PDAC-YFP cells, and the liver was analyzed after 10 days. **a**, Images of the liver showing metastatic lesions (yellow, CK19) and Ki-67 (purple). Scale bars, 4 mm (left) and 200 μ m (right). **b**, Quantification of lesions (left) and Ki-67⁺ tumor cells (right). Data pooled from three experiments (**a**, **b**). For **c** and **d**, $n = 9$ and 13 for control mice and $n = 6$ and 13 for NTB KPC mice intrasplenically injected with PBS and PDAC (PDA.69). **c**,

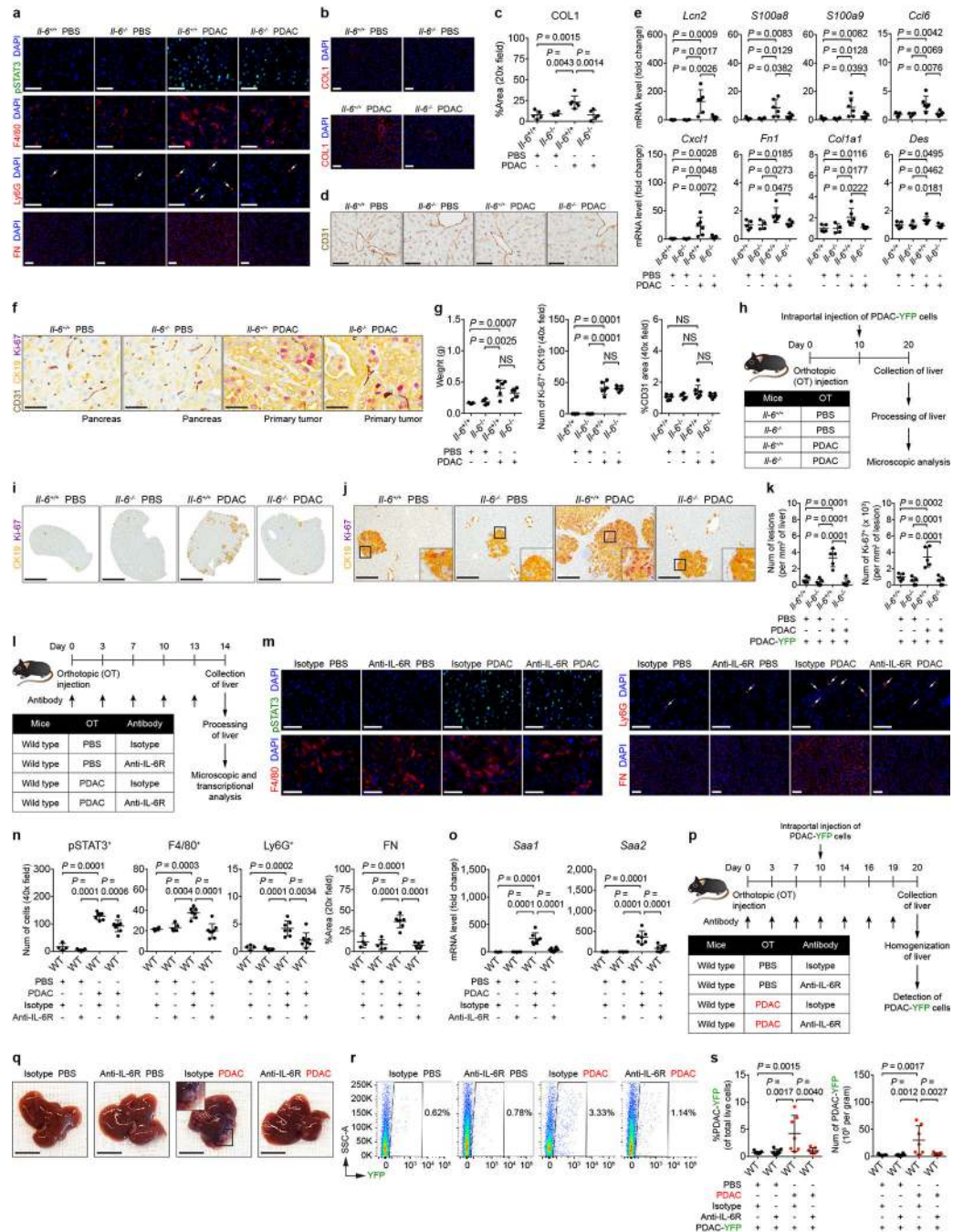
Images of the liver (top) and metastatic lesions in the liver (stained with Pdx1). Scale bars, 1 cm (top) and 50 μ m (bottom). **d**, Liver weights and mRNA levels of *Pdx1* in the liver relative to *Gapdh*. Data pooled from five experiments (**c**, **d**). **e**, Study design for **f** and **g**. Wild type mice were injected with PBS or PDAC cells and then injected with PDAC-YFP cells on day 10. The liver was harvested at 2 hours (**j**, $n = 4$ for both groups) or 24 hours (**k**, $n = 5$ for both groups) after intraportal injection. **f**, **g**, Images and quantification of tumor cells in the liver. Scale bars, 50 μ m. Data representative of one experiment (**e-g**). **h**, Study design for **i-l** ($n = 4$ for both groups). **i**, Images of the liver and flow cytometric analysis. Scale bars, 1 cm. **j**, Quantification of PDAC-YFP cells. **k**, **l**, Images of the liver showing metastatic lesions (yellow, CK19) and Ki-67 (purple). Scale bars, 4 mm (**k**) and 200 μ m (**l**). Data representative of at least three independent experiments (**h-l**). **m**, Study design for **n** and **o** ($n = 5$ for both groups). **n**, Gating strategy for identification of T cell subsets. Images from flow cytometric analysis of cells isolated from the liver of a wild type mouse are shown. EM, effector memory. **o**, Quantification of CD4⁺ T cell subsets (top) and CD8⁺ T cell subsets (bottom) in the liver. Data representative of two independent experiments (**m-o**). For **p-s**, wild type mice were orthotopically injected with PBS or PDAC cells ($n = 4$ for both groups). One group received anti-CD4 and anti-CD8 antibodies on days 8 and 13. Both groups were intraportally injected with PDAC-YFP cells on day 10. **p**, Flow cytometric analysis of the peripheral blood and quantification of CD4⁺ and CD8⁺ T cells. **q**, Images of the liver, flow cytometric analysis, and quantification of PDAC-YFP cells. Scale bars, 1 cm. **r**, Images of the liver showing metastatic lesions (yellow, CK19), Ki-67 (purple, top), and CD4⁺ cells (purple) and CD8⁺ cells (brown, bottom). Scale bars, 200 μ m (top) and 50 μ m (bottom). **s**, Quantification of lesions and Ki-67⁺ tumor cells (top) and CD4⁺ cells and CD8⁺ cells (bottom). Data representative of one experiment (**p-s**). Statistical significance was calculated using one-way ANOVA (**d**) or two-tailed Mann-Whitney test (all other panels). NS, not significant. Data represented as mean \pm s.d.



Extended Data Figure 3 | Primary PDAC development induces expression of myeloid chemoattractants and activates STAT3 signaling in the liver.

a, Study design for **b-e** ($n = 5$ for both groups for **b-d** and $n = 10$ and 9 for control mice and NTB KPC mice for **e**). **b**, Heat map. **c**, Enriched biological processes in the liver of NTB KPC mice. **d**, FPKM values of chemoattractant genes in the liver. **e**, mRNA levels of chemoattractant genes in the liver. Data representative of one experiment (**a-e**). **f**, Enrichment of IL-6/JAK/STAT3 signaling genes in the liver ($n = 5$ for control mice and NTB KPC mice). FDR, false discovery rate; NES, normalized enrichment score. Data representative of one experiment. **g**, Left, images showing hepatocytes (stained for albumin) and pSTAT3. Right, percentage of hepatocytes that are pSTAT3⁺ in control mice ($n = 4$), NTB KPC mice ($n = 5$), and TB KPC mice ($n = 5$). **h**, Left, images of F4/80⁺ cells and pSTAT3. Right, percentage of F4/80⁺ cells that are pSTAT3⁺ in control mice ($n = 9$), NTB KPC mice ($n = 8$), and TB KPC mice ($n = 5$). **i**, Images of F4/80⁺ cells and pSTAT1 in the

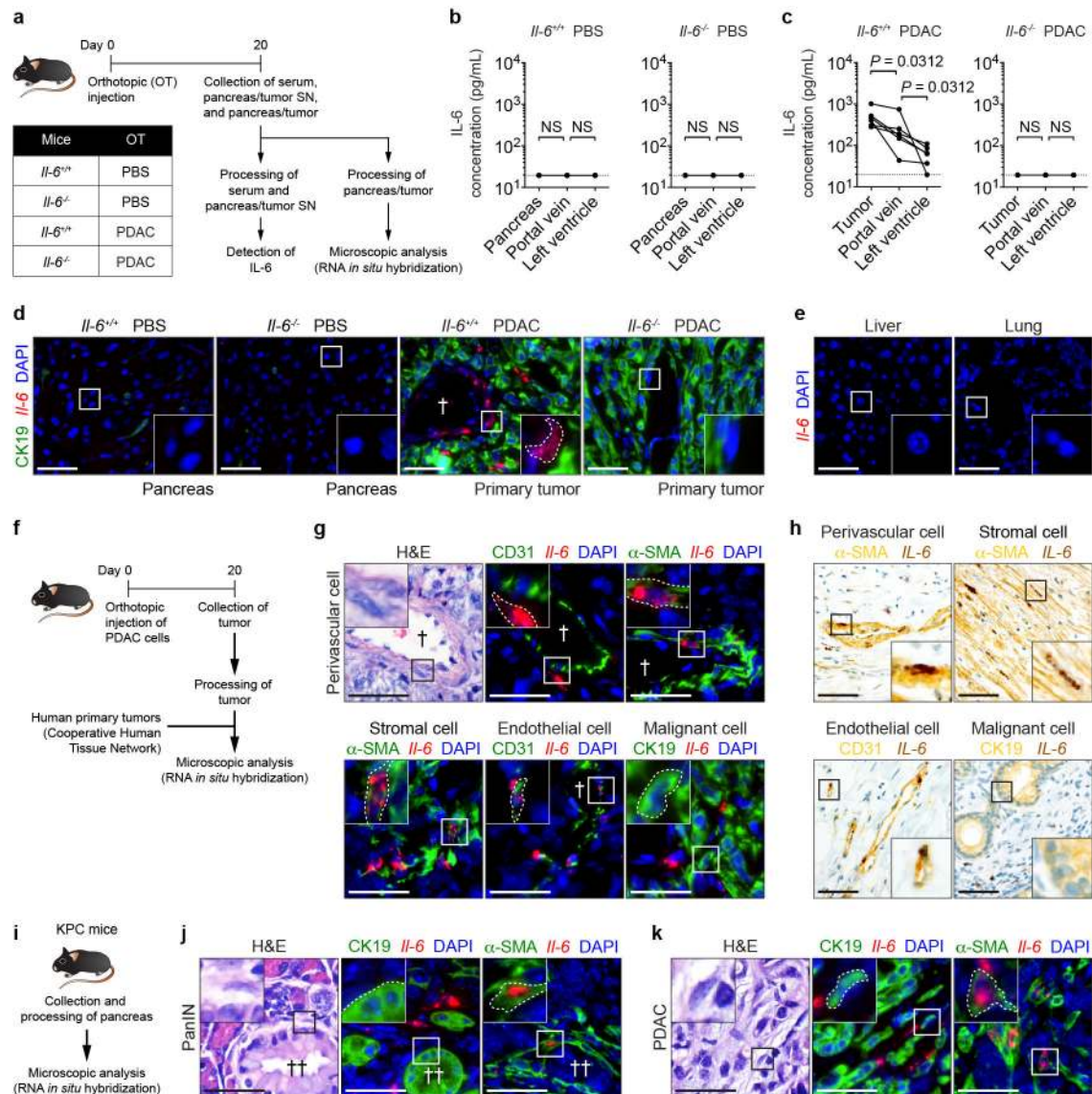
liver of control mice ($n = 9$), NTB KPC mice ($n = 8$), and TB KPC mice ($n = 5$). Data pooled from two experiments (**g-i**). For **j** and **k**, wild type mice were orthotopically injected with PBS ($n = 7$) or PDAC cells ($n = 6$). **j, k**, Left, images of hepatocytes (**j**), F4/80⁺ cells (**k**), and pSTAT3. Right, percentage of hepatocytes (**j**) and F4/80⁺ cells (**k**) that are pSTAT3⁺. Scale bars, 50 μ m. Statistical significance was calculated using ClueGO (b, Ref 34), two-tailed unpaired Student's t test (**d**), GSEA (**f**, Ref 38), one-way ANOVA with Dunnett's test (**g, h**), and two-tailed Mann-Whitney test (all other panels). NS, not significant. Data represented as mean \pm s.d., except **d** and **e**, which are shown as box plots (center line, median; box limits, upper and lower quartiles; whiskers, max and min values).



Extended Data Figure 4 | IL-6 promotes the formation of a pro-metastatic niche in the liver.

For **a-g**, $n = 5$ and 6 for $Il-6^{+/+}$ mice and $n = 4$ and 5 for $Il-6^{-/-}$ mice orthotopically injected with PBS or PDAC cells, respectively. **a**, Images of pSTAT3⁺ cells, myeloid cells, and FN. Arrows indicate Ly6G⁺ cells. **b, c**, Images and quantification of COL1. **d**, Images of sinusoids (brown, stained with CD31) in the liver. **e**, mRNA levels of *Lcn2*, *S100a8*, *S100a9*, *Ccl6*, *Cxcl1*, *Fnl*, *Col1a1*, and *Des* in the liver. **f**, Images of the pancreas and primary tumor stained with CD31 (brown), CK19 (yellow), and Ki-67 (purple). **g**, Quantification of the weight of pancreas/primary tumor (left), number of Ki-67⁺ tumor cells (middle), and

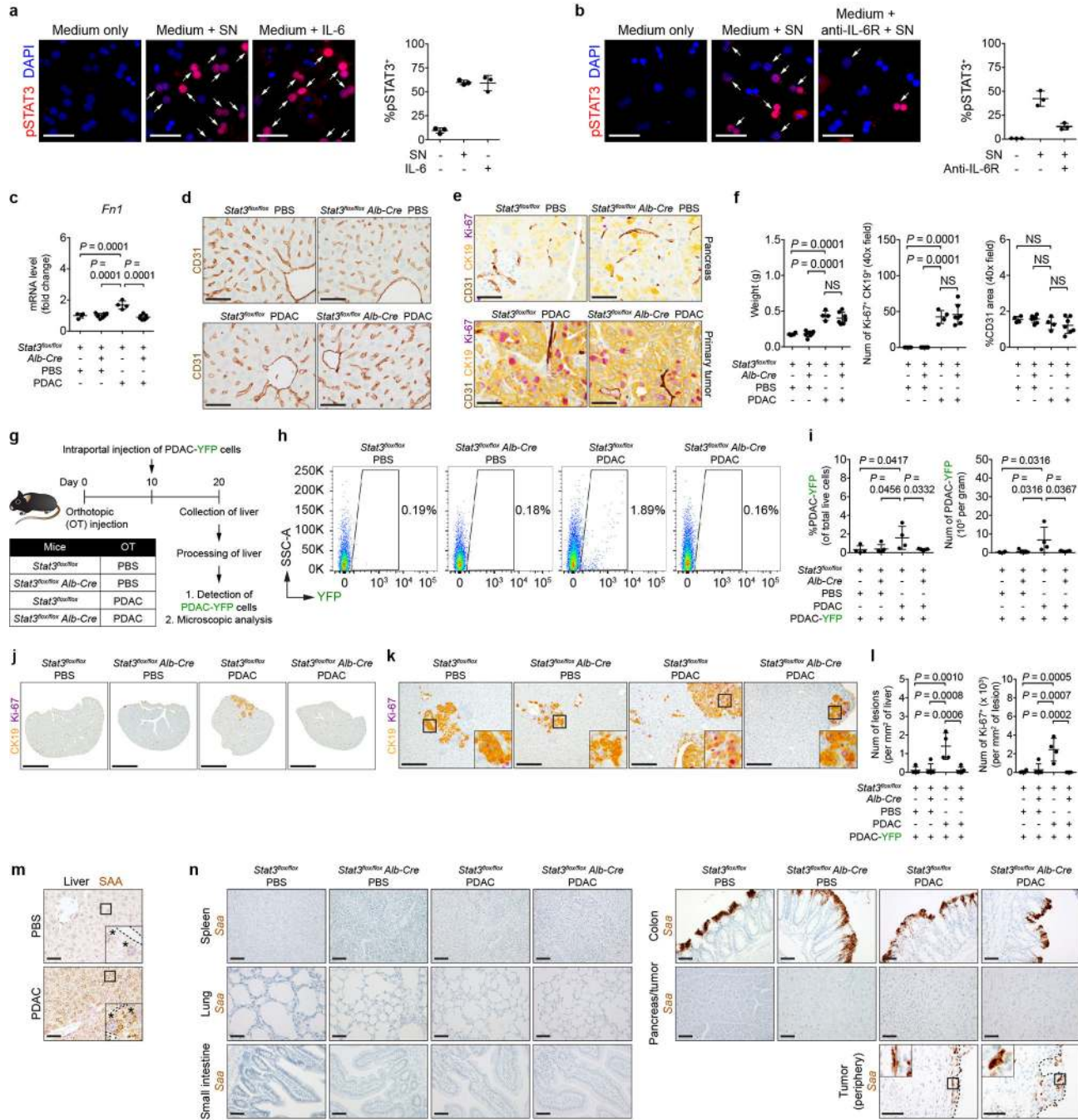
vascular area (right). Data representative of one (**b-d**, *Fnl*, *Col1a1*, and *Des* in **e**, **f**, **g**) or two independent experiments (**a**, all other genes in **e**). **h**, Study design for **i-k** ($n = 5$ for all groups). All groups were injected with PDAC-YFP cells on day 10. **i**, **j**, Images of the liver showing metastatic lesions (yellow, CK19) and Ki-67 (purple). Scale bars, 4 mm (**i**) and 200 μ m (**j**). **k**, Quantification of lesions (left) and Ki-67⁺ tumor cells (right). Data representative of one experiment (**h-k**). **l**, Study design for **m-o** ($n = 4$ and 5 for mice injected with PBS and treated with isotype control or anti-IL-6R antibodies, respectively; $n = 7$ and 8 for mice injected with PDAC cells and treated with isotype control or anti-IL-6R antibodies, respectively, unless indicated otherwise below). **m**, **n**, Images and quantification of pSTAT3⁺ cells, myeloid cells, and FN. For FN, $n = 7$ for mice injected with PDAC cells and treated with anti-IL-6R antibodies. Arrows indicate Ly6G⁺ cells. **o**, mRNA levels of *Saa*. **p**, Study design for **q-s** ($n = 7$ and 8 for mice injected with PBS and treated with isotype control and anti-IL-6R antibodies; $n = 7$ for mice injected with PDAC cells and treated with isotype control and anti-IL-6R antibodies). All groups were injected with PDAC-YFP cells on day 10. **q**, **r**, Images of the liver and flow cytometric analysis. Scale bars, 1 cm. **s**, Quantification of PDAC-YFP cells. Data representative of two independent experiments (**l-s**). Scale bars, 50 μ m unless indicated otherwise. Statistical significance was calculated using one-way ANOVA with Dunnett's test. NS, not significant. Data represented as mean \pm s.d.



Extended Data Figure 5 | Non-malignant cells are the predominant source of IL-6.

a, Study design for **b-e** ($n = 5$ and 6 for *IL-6*^{+/+} mice injected with PBS or PDAC cells, respectively; $n = 4$ and 5 for *IL-6*^{-/-} mice injected with PBS or PDAC cells, respectively). SN, supernatant. **b**, Concentration of IL-6 in pancreas supernatant and serum collected from indicated sites in *IL-6*^{+/+} mice injected with PBS or PDAC cells. **c**, Concentration of IL-6 in pancreatic tumor supernatant and serum collected from indicated sites in *IL-6*^{-/-} mice injected with PBS or PDAC cells. Solid lines indicate data points from individual mice, and dashed lines indicate the lower limit of detection (**b**, **c**). **d**, Images of CK19 and *IL-6* mRNA in the pancreas and primary tumor. **e**, Images of *IL-6* mRNA in the liver and lung of *IL-6*^{+/+} mice injected with PDAC cells. Data representative of two independent experiments (**a-e**). **f**, Study design for **g** and **h** ($n = 4$ for *IL-6*^{+/+} mice injected with PDAC cells and $n = 5$ for human samples). **g**, Images of α -SMA, CD31, CK19, and *IL-6* mRNA in perivascular cells (top), stromal cells (bottom, left), endothelial cells (bottom, middle) and malignant cells (bottom, right) present within the mouse primary tumor. **h**, Images of α -SMA (yellow),

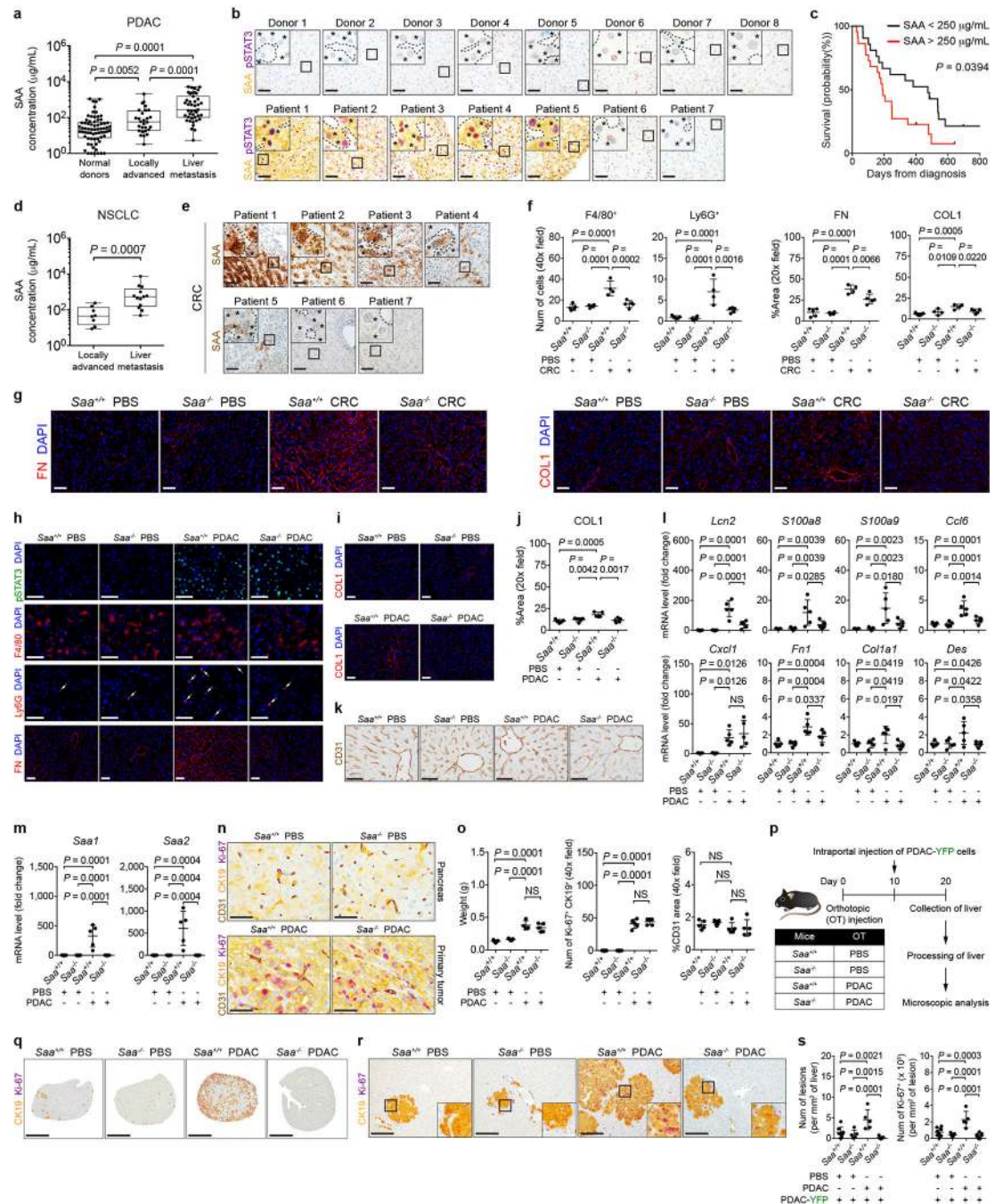
CD31 (yellow), CK19 (yellow), and *IL-6* mRNA (brown) in perivascular cells (top, left), stromal cells (top, right), endothelial cells (bottom, left) and malignant cells (bottom, right) present within the human primary tumor. Data representative of one experiment (**f-h**). **i**, Study design for **j** and **k** ($n = 5$). **j**, **k**, Representative images of α -SMA, CK19, and *IL-6* mRNA detected in PanIN (**j**) and invasive PDAC (**k**). Data representative of one experiment (**i-k**). Scale bars, 50 μ m. Statistical significance was calculated using two-tailed Wilcoxon test. NS, not significant. †, blood vessel; ††, PanIN lesion. Data from individual mice are shown in **b** and **c**.



Extended Data Figure 6 | STAT3 signaling in hepatocytes promotes the formation of a pro-metastatic niche in the liver.

a, b, Representative images and quantification of pSTAT3⁺ hepatocytes ($n = 3$ technical replicates per condition). Arrows indicate pSTAT3⁺ hepatocytes. SN, pancreatic tumor supernatant. Data representative of two independent experiments (**a, b**). For **c-f** and **n**, $n = 4$ for *Stat3^{flox/flox}* mice and $n = 8$ and 7 for *Stat3^{flox/flox} Alb-Cre* mice orthotopically injected with PBS or PDAC cells, respectively. **c**, mRNA levels of *Fn1* in the liver. **d**, Images of sinusoids (brown, stained for CD31) in the liver. **e**, Images of the pancreas and primary

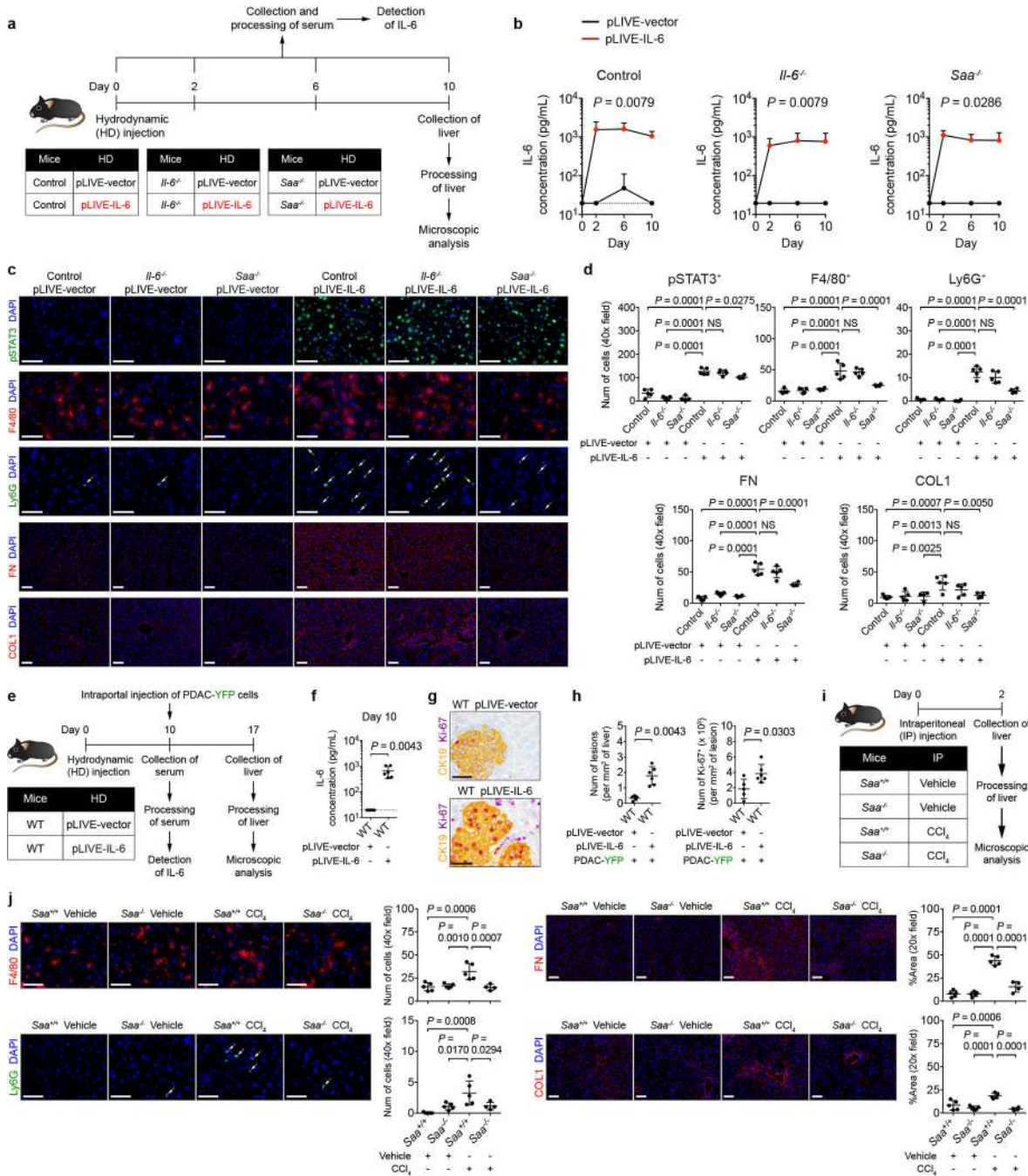
tumor stained for CD31 (brown), CK19 (yellow), and Ki-67 (purple). **f**, Quantification of the weight of pancreas/primary tumor (left), number of Ki-67⁺ tumor cells (middle), and vascular area (right). Data representative of one experiment (**c-f**). **g**, Study design for **h-l** ($n = 4$ and 5 for *Stat3^{flox/flox}* mice and *Stat3^{flox/flox} Alb-Cre* mice, respectively). All groups were injected with PDAC-YFP cells on day 10. **h**, Flow cytometric analysis. **i**, Quantification of PDAC-YFP cells. **j, k**, Images of the liver showing metastatic lesions (yellow, CK19) and Ki-67 (purple). Scale bars, 4 mm (**j**) and 200 μ m (**k**). **l**, Quantification of lesions (left) and Ki-67⁺ tumor cells (right). Data representative of one experiment (**g-l**). **m**, Images of SAA detected by immunohistochemistry (brown, $n = 5$ for wild type mice orthotopically injected with PBS or PDAC cells). Dashed lines and asterisks indicate sinusoids and hepatocytes, respectively. **n**, Images of *Saa* mRNA (brown) detected by RNA *in situ* hybridization. Data representative of one experiment (**m, n**). Scale bars, 50 μ m unless indicated otherwise. Statistical significance was calculated using one-way ANOVA with Dunnett's test. NS, not significant. Data represented as mean \pm s.d.



Extended Data Figure 7 | SAA promotes the formation of a pro-metastatic niche in the liver.

a, Concentration of circulating SAA in normal donors ($n = 69$), patients with locally advanced PDAC ($n = 28$), and patients with liver metastases ($n = 43$). Data represented as a box plot (center line, median; box limits, upper and lower quartiles; whiskers, max and min values). **b**, Images of SAA (yellow) and pSTAT3 (purple) in the liver of normal donors and PDAC patients with liver metastases. Dashed lines and asterisks indicate sinusoids and hepatocytes, respectively. **c**, Kaplan-Meier survival curve for PDAC patients with liver metastases with low (< 250 mg/mL, black, $n = 21$) and high (> 250 mg/mL, red, $n = 22$)

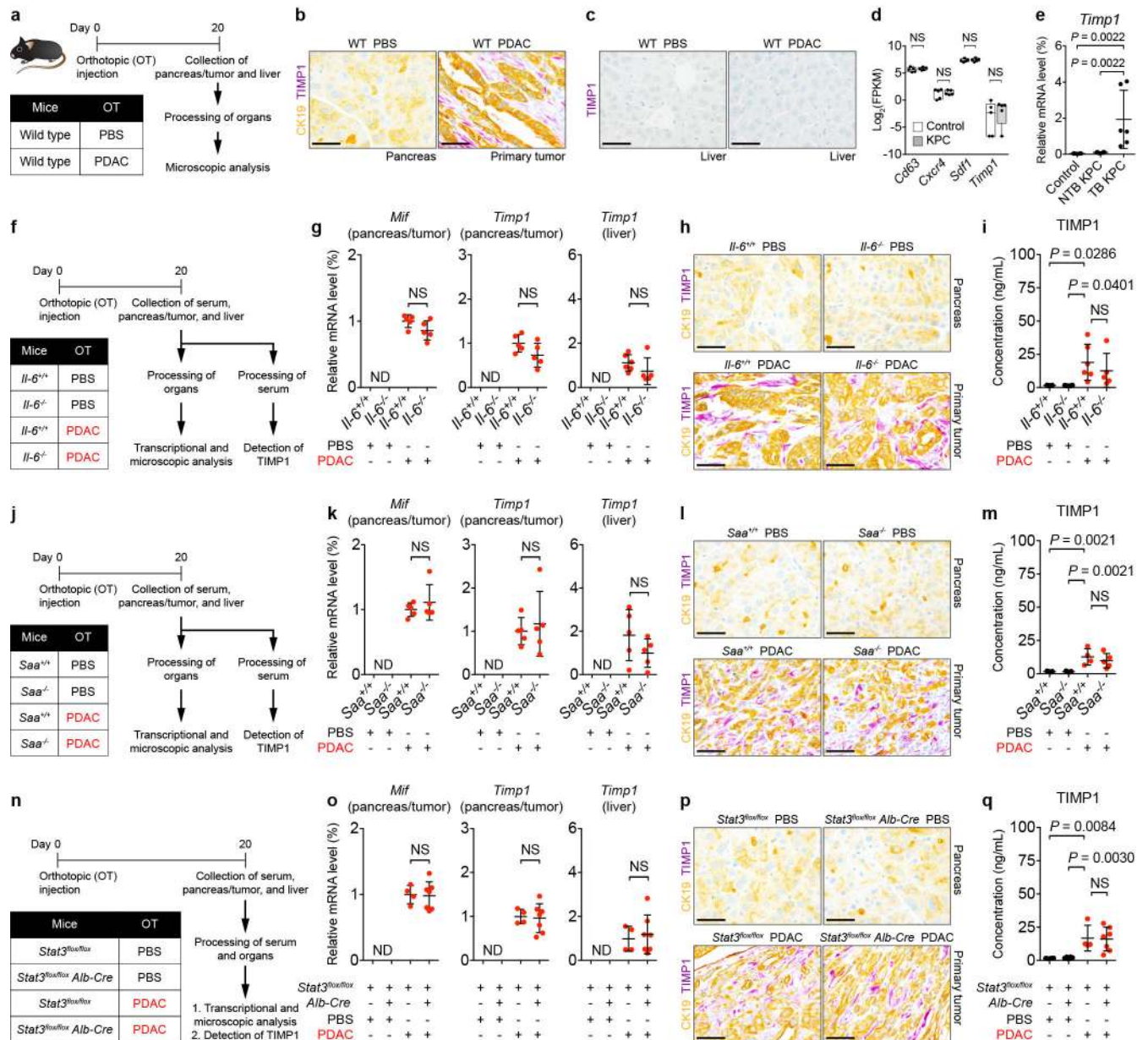
levels of circulating SAA. **d**, Concentration of circulating SAA in patients with locally advanced non-small cell lung carcinoma (NSCLC, $n = 8$) and NSCLC patients with liver metastases ($n = 13$). Data shown as a box plot (center line, median; box limits, upper and lower quartiles; whiskers, max and min values). **e**, Images of SAA (brown) in the liver of CRC patients with liver metastases. Dashed lines and asterisks indicate sinusoids and hepatocytes. Data representative of one experiment (**a-e**). For **f** and **g**, $n = 5$ and 4 for $Saa^{+/+}$ mice and $n = 4$ and 5 for $Saa^{-/-}$ mice orthotopically injected with PBS or CRC cells (MC-38), respectively. **f**, Quantification of myeloid cells, FN, and COL1. **g**, Images of FN (left) and COL1 (right). Data representative of one experiment (**f, g**). For **h-o**, $n = 5$ for all groups unless indicated otherwise. **h**, Images of pSTAT3+ cells, myeloid cells, and FN. **i, j**, Images and quantification of COL1. **k**, Images of sinusoids (brown, CD31) in the liver. **l**, mRNA levels of *Lcn2*, *S100a8*, *S100a9*, *Ccl6*, *Cxcl1*, *Fnl*, *Colla1*, and *Des* in the liver. **m**, mRNA levels of *Saa1* and *Saa2*. **n**, Images of the pancreas and primary tumor stained for CD31 (brown), CK19 (yellow), and Ki-67 (purple). **o**, Quantification of the weight of pancreas/primary tumor (left), number of Ki-67+ tumor cells (middle), and vascular area (right). For weight, $n = 4$ for $Saa^{+/+}$ mice injected with PDAC cells. Data representative of one (**i-k**, *Fnl*, *Colla1*, and *Des* in **l**, **n**, **o**) or two independent experiments (**h**, all other genes in **l**, **m**). **p**, Study design for **q-s** ($n = 8$ and 5 for $Saa^{+/+}$ mice and $n = 5$ and 7 for $Saa^{-/-}$ mice injected with PBS or PDAC cells, respectively). All groups were injected with PDAC-YFP cells on day 10. **q, r**, Images of the liver showing metastatic lesions (yellow, CK19) and Ki-67 (purple). Scale bars, 4 mm (**q**) and 200 μ m (**r**). **s**, Quantification of lesions (left) and Ki-67+ tumor cells (right). Data representative of one experiment (**p-s**). Scale bars, 50 μ m unless indicated otherwise. Statistical significance was calculated using two-sided Mann-Whitney test (**a, d**), Mantel-Cox test (**c**), and one-way ANOVA with Dunnett's test (all other panels). NS, not significant. Data represented as mean \pm s.d. unless indicated otherwise.



Extended Data Figure 8 | SAA is a downstream mediator of IL-6 signaling that drives myeloid cell accumulation and fibrosis within the liver.

a, Study design for **b-d** ($n = 5$ for all groups, except $n = 4$ for $Saa^{-/-}$ mice). **b**, Concentration of IL-6 in the serum collected from control mice (left), $Il-6^{-/-}$ mice (middle), and $Saa^{-/-}$ mice (right) on indicated days. **c, d**, Images and quantification of pSTAT3⁺ cells, myeloid cells, FN, and COL1. Arrows indicate Ly6G⁺ cells. Data representative of one experiment (**a-d**). **e**, Study design ($n = 5$ for mice injected with pLIVE-vector; $n = 6$ for mice injected with pLIVE-IL-6). **f**, Concentration of IL-6 in the serum. **g**, Images of the liver showing

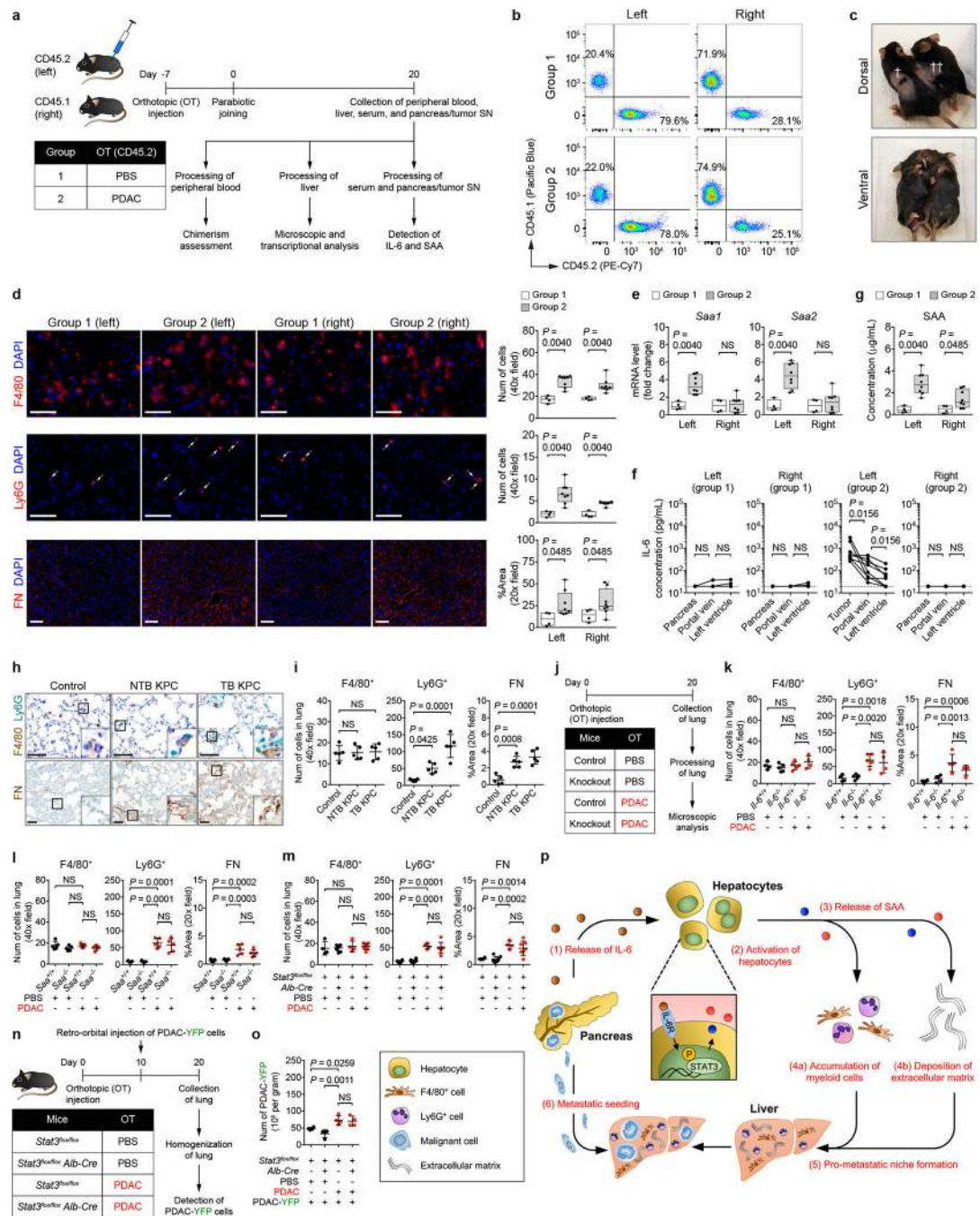
metastatic lesions (yellow, CK19) and Ki-67 (purple). **h**, Quantification of lesions (left) and Ki-67+ tumor cells (right). Data representative of one experiment (**e-h**). **i**, Study design ($n = 5$ for all groups, except $n = 4$ for *Saa*^{-/-} mice injected with CCl₄). **j**, Images and quantification of myeloid cells, FN, and COL1. Arrows indicate Ly6G⁺ cells. Dashed lines indicate the lower limit of detection (**b, f**). Scale bars, 50 μ m. Statistical significance was calculated using two-tailed Mann-Whitney test (**b, f, h**) or one-way ANOVA (all other panels). NS, not significant. Data represented as mean \pm s.d. or mean \pm s.d.



Extended Data Figure 9 | IL-6/STAT3/SAA signaling axis does not impact expression of MIF and TIMP1.

a, Study design ($n = 5$ and 4 for mice injected with PBS and PDAC cells). **b, c**, Images of CK19 (yellow) and TIMP1 (purple) in the pancreas, primary tumor, and liver. Data

representative of at least three independent experiments (**a-c**). **d**, FPKM values of genes in the liver of control mice ($n = 5$) and NTB KPC mice ($n = 5$) obtained from QuantSeq 3' mRNA sequencing. Data represented as box plots (center line, median; box limits, upper and lower quartiles; whiskers, max and min values). **e**, mRNA levels of *Timp1* in the liver of control mice ($n = 6$), NTB KPC mice ($n = 7$), and TB KPC mice ($n = 6$) relative to *Actb*. Data representative of one experiment (**d, e**). **f, j, n**, Study designs. For **f**, $n = 5$ for *Il-6^{+/+}* mice injected with PBS and $n = 5$ or 6 for *Il-6^{+/+}* mice injected with PDAC cells. $n = 4$ and 5 for *Il-6^{-/-}* mice injected with PBS or PDAC cells, respectively. For **j**, $n = 5$ for all groups, except $n = 4$ or 5 for *Saa^{+/+}* injected with PDAC cells. For **n**, $n = 4$ for *Stat3^{flox/flox}* mice and $n = 8$ and 7 for *Stat3^{flox/flox} Alb-Cre* mice injected with PBS or PDAC cells, respectively. **g, k, o**, mRNA levels of *Mif* and *Timp1* in the indicated organs relative to *Actb*. **h, l, p**, Images of CK19 (yellow) and TIMP1 (purple) in the pancreas and primary tumor. **i, m, q**, Concentration of TIMP1 in the serum. Data representative of one experiment (**f-q**). Scale bars, 50 μ m. Statistical significance was calculated using one-way ANOVA with Dunnett's test (**i, m, q**) or two-tailed Mann-Whitney test (all other panels). NS, not significant. ND, not detected. Data represented as mean \pm s.d. unless indicated otherwise.



Extended Data Figure 10 | Primary PDAC development induces a systemic response that promotes the formation of a pro-metastatic niche in the liver.

a, Study design for **b-g** ($n = 4$ and 8 for CD45.2 mice injected with PBS (group 1) or PDAC cells (group 2)). SN, supernatant. **b**, Assessment of chimerism in parabiotically joined mice. Flow cytometric analysis of the peripheral blood gated on CD45.1⁺ and CD45.2⁺ cells as a percentage of CD45⁺ cells. **c**, Dorsal (top) and ventral (bottom) views of parabiotically joined mice. †, site of laparotomy for orthotopic injection; ††, skin suture for parabiotic joining. **d**, Images and quantification of myeloid cells and FN. Arrows indicate Ly6G⁺ cells.

e, mRNA levels of *Saa*. **f**, Concentration of IL-6 in pancreas supernatant and serum. Solid lines indicate data points from individual mice. Dashed lines indicate the lower limit of detection. **g**, Concentration of circulating SAA. Data representative of one (**f**, **g**) or two independent experiments (**a-e**). For **h** and **i**, $n = 5$ for all groups. **h**, Images of myeloid cells and FN in the lung of control mice, NTB KPC mice, and TB KPC mice. **i**, Quantification of myeloid cells and FN. Data representative of one experiment (**h**, **i**). **j**, Study design for **k-m**. For **k**, $n = 4$ and 5 for *Il-6^{+/+}* mice and $n = 5$ and 4 for *Il-6^{-/-}* mice injected with PBS or PDAC cells, respectively. For **l**, $n = 5$ for all groups. For **m**, $n = 4$ for *Stat3^{fllox/fllox}* mice and $n = 8$ and 7 for *Stat3^{fllox/fllox} Alb-Cre* mice injected with PBS or PDAC cells, respectively. **k**, **l**, **m**, Quantification of myeloid cells and FN. Data representative of one experiment (**j-m**). **n**, Study design for **o** ($n = 4$ for all groups of mice). All groups of mice were injected with PDAC-YFP cells on day 10. **o**, Quantification of PDAC-YFP cells. Data representative of one experiment (**n**, **o**). **p**, conceptual model. Scale bars, 50 μ m. Statistical significance was calculated using two-sided Mann-Whitney test (**d**, **e**, **g**), two-sided Wilcoxon test (**f**), and one-way ANOVA with Dunnett's test (all other panels). NS, not significant. Data represented as mean \pm s.d, except **d**, **e**, and **g**, which are shown as box plots (center line, median; box limits, upper and lower quartiles; whiskers, max and min values). Data from individual mice are shown in **f**.

Supplementary Material

Refer to Web version on PubMed Central for supplementary material.

Acknowledgements

We thank members of the K. S. Zaret laboratory for assistance with isolation and culture of primary hepatocytes and members of the Genomics Facility (Wistar Institute) and the Molecular Pathology and Imaging Core (University of Pennsylvania) for technical support. We thank E. J. Wherry, D. J. Powell, J. R. Conejo-Garcia, I. E. Brodsky, and E. L. Stone for discussions and advice. We thank the Mayo Clinic Arizona for provision of liver tissue sections collected from patients with pancreatic cancer. This work was supported by National Institutes of Health grants F30 CA196106 (J.W.L.), T32 HL007439 (J.W.L.), T32 CA009140 (M.L.S.), R01 CA197916 (G.L.B.), R01 HL134731 (N.R.W. and F.C.d.B.), the University of Pennsylvania Molecular Pathology and Imaging Core of the Center for Molecular Studies in Digestive and Liver Diseases grant P30 DK050306, the 2015 Pancreatic Cancer Action Network-AACR Career Development Award 15-20-25-BEAT supported by an anonymous foundation (G.L.B.), the 2017 Stand Up to Cancer (SU2C) Innovative Research Grant SU2C-AACR-IRG 13-17 (G.L.B.), a Research Support Grant from the University of Kentucky Office of the Vice President for Research (N.R.W.), the American Surgical Association Foundation Fellowship (P.M.P.), the University of Pennsylvania Pancreatic Cancer Research Center (E.L.C.), and the Abramson Cancer Center Translational Centers of Excellence (E.L.C.).

References

1. Hidalgo M Pancreatic cancer. *N. Engl. J. Med* 362, 1605–1617 (2010). [PubMed: 20427809]
2. Becker A et al. Extracellular vesicles in cancer: cell-to-cell mediators of metastasis. *Cancer Cell* 30, 836–848 (2016). [PubMed: 27960084]
3. Sceney J, Smyth MJ & Möller A The pre-metastatic niche: finding common ground. *Cancer Metastasis Rev.* 32, 449–464 (2013). [PubMed: 23636348]
4. Hingorani SR et al. *Trp53R^{172H}* and *Kras^{G12D}* cooperate to promote chromosomal instability and widely metastatic pancreatic ductal adenocarcinoma in mice. *Cancer Cell* 7, 469–483 (2005). [PubMed: 15894267]
5. Lee JW, Komar CA, Bengsch F, Graham K & Beatty GL Genetically engineered mouse models of pancreatic cancer: the KPC model (LSL-KrasG12D/+;LSL-Trp53R172H/+;Pdx-1-Cre), its variants,

- and their application in immuno-oncology drug discovery. *Curr. Protoc. Pharmacol* 73, 14.39.1–14.39.20 (2016). [PubMed: 27248578]
6. Rhim AD et al. EMT and dissemination precede pancreatic tumor formation. *Cell* 148, 349–361 (2012). [PubMed: 22265420]
 7. Grünwald B et al. Pancreatic pre-malignant lesions secrete TIMP1, which activates hepatic stellate cells via CD63 signaling to create a pre-metastatic niche in the liver. *Gastroenterology* 151, 1011–1024 (2016). [PubMed: 27506299]
 8. Seubert B et al. Tissue inhibitor of metalloproteinases (TIMP)-1 creates a premetastatic niche in the liver through SDF-1/CXCR4-dependent neutrophil recruitment in mice. *Hepatology* 61, 238–248 (2015). [PubMed: 25131778]
 9. Hoshino A et al. Tumour exosome integrins determine organotropic metastasis. *Nature* 527, 329–335 (2015). [PubMed: 26524530]
 10. Costa-Silva B et al. Pancreatic cancer exosomes initiate pre-metastatic niche formation in the liver. *Nat. Cell Biol* 17, 816–826 (2015). [PubMed: 25985394]
 11. Kowanzet M et al. Granulocyte-colony stimulating factor promotes lung metastasis through mobilization of Ly6G+Ly6C+ granulocytes. *Proc. Natl. Acad. Sci. USA* 107, 21248–21255 (2010). [PubMed: 21081700]
 12. Hiratsuka S et al. The S100A8–serum amyloid A3–TLR4 paracrine cascade establishes a pre-metastatic phase. *Nat. Cell Biol* 10, 1349–1355 (2008). [PubMed: 18820689]
 13. Hiratsuka S, Watanabe A, Aburatani H & Maru Y Tumour-mediated upregulation of chemoattractants and recruitment of myeloid cells predetermines lung metastasis. *Nat. Cell Biol* 8, 1369–1375 (2006). [PubMed: 17128264]
 14. Schmidt-Arras D & Rose-John S IL-6 pathway in the liver: From physiopathology to therapy. *J. Hepatol* 64, 1403–1415 (2016). [PubMed: 26867490]
 15. Long KB et al. IL6 receptor blockade enhances chemotherapy efficacy in pancreatic ductal adenocarcinoma. *Mol. Cancer Ther* 16, 1898–1908 (2017). [PubMed: 28611107]
 16. Lesina M et al. Stat3/Socs3 activation by IL-6 transsignaling promotes progression of pancreatic intraepithelial neoplasia and development of pancreatic cancer. *Cancer Cell* 19, 456–469 (2011). [PubMed: 21481788]
 17. Fukuda A et al. Stat3 and MMP7 contribute to pancreatic ductal adenocarcinoma initiation and progression. *Cancer Cell* 19, 441–455 (2011). [PubMed: 21481787]
 18. Corcoran RB et al. STAT3 plays a critical role in KRAS-induced pancreatic tumorigenesis. *Cancer Res.* 71, 5020–5029 (2011). [PubMed: 21586612]
 19. Eckhardt ER et al. Intestinal epithelial serum amyloid A modulates bacterial growth in vitro and pro-inflammatory responses in mouse experimental colitis. *BMC Gastroenterol.* 10, 1–9 (2010). [PubMed: 20064220]
 20. Urieli-Shoval S, Linke RP & Matzner Y Expression and function of serum amyloid A, a major acute-phase protein, in normal and disease states. *Curr. Opin. Hematol* 7, 64–69 (2000). [PubMed: 10608507]
 21. Chan-Seng-Yue M et al. A renewed model of pancreatic cancer evolution based on genomic rearrangement patterns. *Nature* 538, 1–20 (2016).
 22. Yachida S et al. Distant metastasis occurs late during the genetic evolution of pancreatic cancer. *Nature* 467, 1114–1117 (2010). [PubMed: 20981102]
 23. Reichert M et al. Regulation of epithelial plasticity determines metastatic organotropism in pancreatic cancer. *Dev. Cell* 45, 696–711 (2018). [PubMed: 29920275]
 24. de Beer MC et al. Impact of serum amyloid A on high density lipoprotein composition and levels. *J. Lipid Res* 51, 3117–3125 (2010). [PubMed: 20667817]
 25. Liang WS et al. Genome-wide characterization of pancreatic adenocarcinoma patients using next generation sequencing. *PLoS ONE* 7, 1–20 (2012).
 26. Long KB et al. IFN γ and CCL2 cooperate to redirect tumor-infiltrating monocytes to degrade fibrosis and enhance chemotherapy efficacy in pancreatic carcinoma. *Cancer Disc.* 6, 400–413 (2016).
 27. Soares KC et al. A preclinical murine model of hepatic metastases. *J. Vis. Exp* 91, 1–10 (2014).

28. Ma Y, Gao M, Sun H & Liu D Interleukin-6 gene transfer reverses body weight gain and fatty liver in obese mice. *Biochim. Biophys. Acta* 1852, 1001–1011 (2015). [PubMed: 25660446]
29. Tseng W, Leong X & Engleman E Orthotopic mouse model of colorectal cancer. *J. Vis. Exp* 10, 1–4 (2007).
30. Klaas M et al. The alterations in the extracellular matrix composition guide the repair of damaged liver tissue. *Sci. Rep* 6, 1–12 (2016). [PubMed: 28442746]
31. Webb NR et al. Deficiency of endogenous acute-phase serum amyloid A protects apoE^{−/−} mice from angiotensin II-induced abdominal aortic aneurysm formation. *Arterioscler. Thromb. Vasc. Biol* 35, 1156–1165 (2015). [PubMed: 25745063]
32. Sun Y et al. Sudan black B reduces autofluorescence in murine renal tissue. *Arch. Pathol. Lab. Med* 135, 1335–1342 (2011). [PubMed: 21970489]
33. Kalbasi A et al. Tumor-derived CCL2 mediates resistance to radiotherapy in pancreatic ductal adenocarcinoma. *Clin. Cancer Res* 23, 137–148 (2017). [PubMed: 27354473]
34. Bindea G et al. ClueGO: a Cytoscape plug-in to decipher functionally grouped gene ontology and pathway annotation networks. *Bioinformatics* 25, 1091–1093 (2009). [PubMed: 19237447]
35. Bindea G, Galon J & Mlecnik B CluePedia Cytoscape plugin: pathway insights using integrated experimental and in silico data. *Bioinformatics* 29, 661–663 (2013). [PubMed: 23325622]
36. Shannon P et al. Cytoscape: a software environment for integrated models of biomolecular interaction networks. *Genome Res.* 13, 2498–2504 (2003). [PubMed: 14597658]
37. The Gene Ontology Consortium. Expansion of the gene ontology knowledgebase and resources. *Nucleic Acids Res.* 45, D331–D338 (2017). [PubMed: 27899567]
38. Ashburner M et al. Gene ontology: tool for the unification of biology. The Gene Ontology Consortium. *Nat. Genet* 25, 25–29 (2000). [PubMed: 10802651]
39. Subramanian A et al. Gene set enrichment analysis: a knowledge-based approach for interpreting genome-wide expression profiles. *Proc. Natl. Acad. Sci. USA* 102, 15545–15550 (2005). [PubMed: 16199517]

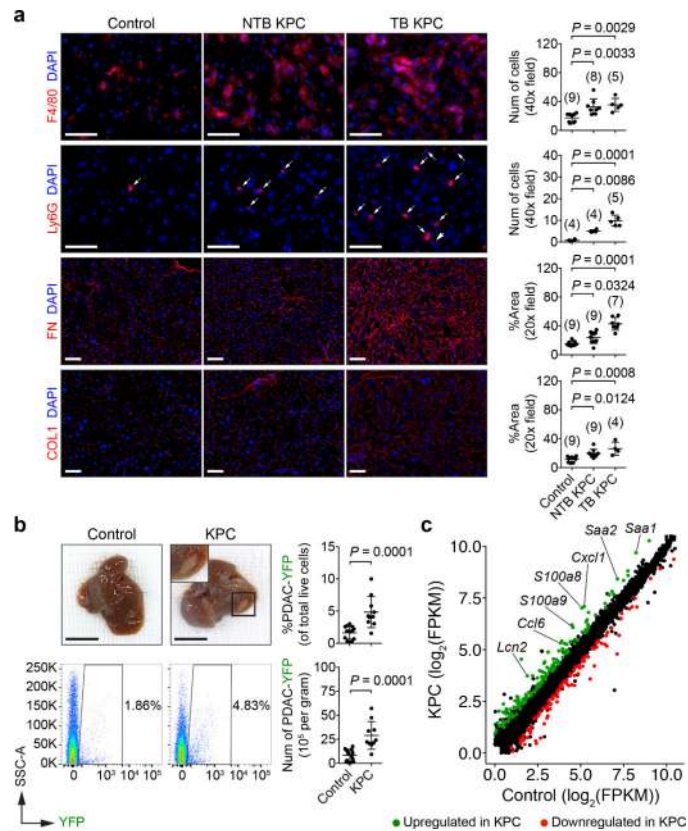


Figure 1 | Primary PDAC development induces a pro-metastatic niche in the liver.

a, Images and quantification of myeloid cells, FN, and COL1 in the liver. Arrows indicate Ly6G⁺ cells. Numbers in parentheses indicate the number (*n*) of mice. Data pooled from two experiments. **b**, Images of the liver and quantification of PDAC-YFP cells. Control mice (*n* = 14) and NTB KPC mice (*n* = 10) were intrasplenically injected with PDAC-YFP cells, and the liver was analyzed after 10 days. Data representative of two independent experiments. **c**, Scatter plot of transcriptome data. FPKM, fragments per kilobase of exon per million mapped fragments (*n* = 5 for both groups). Scale bars, 50 μ m (**a**) and 1 cm (**b**). Statistical significance was calculated using one-way ANOVA with Dunnett's test (**a**) and two-tailed Mann-Whitney test (**b**). Data represented as mean \pm s.d.

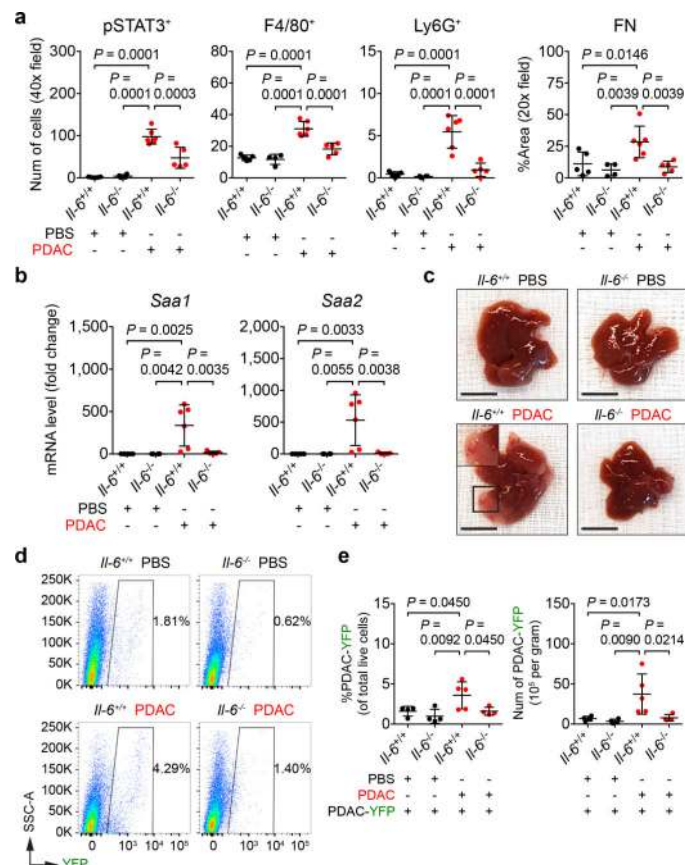


Figure 2 | IL-6 is necessary for the establishment of a pro-metastatic niche in the liver. For **a** and **b**, $n = 5$ and 6 for $Il-6^{+/+}$ mice and $n = 4$ and 5 for $Il-6^{-/-}$ mice orthotopically injected with PBS or PDAC cells, respectively. **a**, Quantification of pSTAT3⁺ cells, myeloid cells, and FN. **b**, mRNA levels of *Saa* in the liver. For **c-e**, $n = 4$ and 5 for $Il-6^{+/+}$ mice and $n = 4$ for $Il-6^{-/-}$ mice orthotopically injected with PBS or PDAC cells, respectively. All groups were intraportally injected with PDAC-YFP cells on day 10. **c**, **d**, Images of liver and flow cytometric analysis. **e**, Quantification of PDAC-YFP cells. Data representative of two independent experiments (**a-e**). Scale bars, 1 cm. Statistical significance was calculated using one-way ANOVA with Dunnett's test. Data represented as mean \pm s.d.

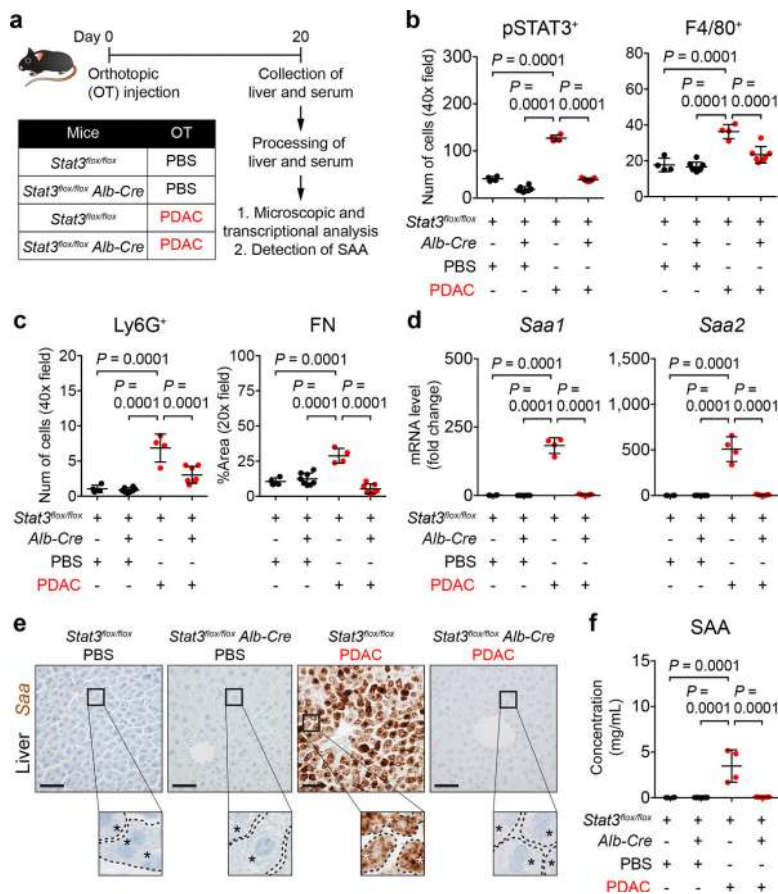


Figure 3 |. STAT3 signaling in hepatocytes orchestrates the formation of a pro-metastatic niche in the liver.
a, Study design for **b-f** ($n = 4$ for *Stat3^{flx/flx}* mice injected with PBS or PDAC cells; $n = 8$ and 7 for *Stat3^{flx/flx} Alb-Cre* mice injected with PBS or PDAC cells, respectively). **b, c**, Quantification of pSTAT3⁺ cells, myeloid cells, and FN. **d**, mRNA levels of *Saa* in the liver. **e**, Images of *Saa*. Dashed lines and asterisks indicate sinusoids and hepatocytes. **f**, Concentration of circulating SAA. Data representative of two independent experiments (**a-f**). Scale bars, 50 μ m. Statistical significance was calculated using one-way ANOVA with Dunnett's test. Data represented as mean \pm s.d.

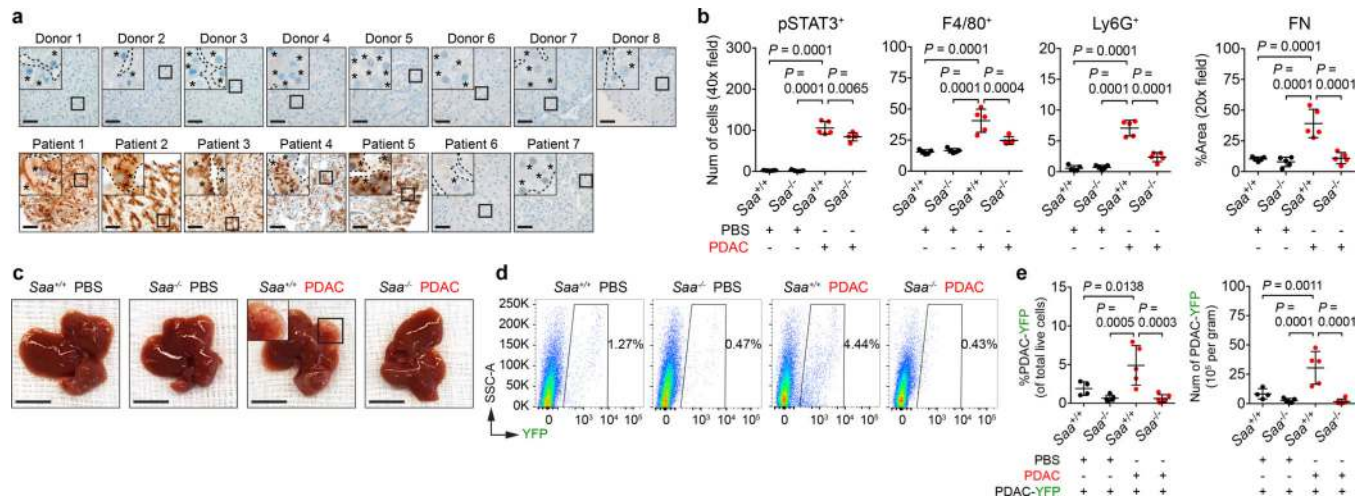


Figure 4 |. SAA is a critical determinant of liver metastasis.

a, Images of SAA in the liver of normal donors (top) and PDAC patients with liver metastases (bottom). Dashed lines and asterisks indicate sinusoids and hepatocytes. Data representative of one experiment. **b**, Quantification of pSTAT3⁺ cells, myeloid cells, and FN ($n = 5$ for all groups orthotopically injected with PBS or PDAC cells). For **c-e**, $n = 4$ and 5 for *Saa*^{+/+} mice and $n = 5$ and 6 for *Saa*^{-/-} mice orthotopically injected with PBS or PDAC cells, respectively. All groups were intraportally injected with PDAC-YFP cells on day 10. **c**, **d**, Images of liver and flow cytometric analysis. **e**, Quantification of PDAC-YFP cells. Data representative of two independent experiments (**b-e**). Scale bars, 50 μ m (**a**) and 1 cm (**c**). Statistical significance was calculated using one-way ANOVA with Dunnett's test. Data represented as mean \pm s.d.